This is a repository copy of *Radiative neutron capture on Pu 242 in the resonance region at the CERN n-TOF-EAR1 facility*.

White Rose Research Online URL for this paper:
https://eprints.whiterose.ac.uk/131338/

Version: Published Version

Article:

Radiative neutron capture on ^{242}Pu in the resonance region at the CERN n_TOF-EAR1 facility

J. Lerendegui-Marco,[1] C. Guerrero,[1,*] E. Mendoza,[2] J. M. Quesada,[1] K. Eberhardt,[3] A. R. Junghans,[4] M. Krtička,[5] O. Aberle,[6]
J. Andrzejewski,[7] L. Audouin,[8] V. Bécares,[2] M. Bacak,[9] J. Balibrea,[2] M. Barbagallo,[10] S. Barros,[11] F. Bečvář,[5] C. Beinrucker,[12]
E. Berthoumieux,[13] J. Billowes,[14] D. Bosnar,[15] M. Brugger,[6] M. Caamaño,[16] F. Calviño,[17] M. Calviani,[6] D. Cano-Ott,[2]
R. Cardella,[6] A. Casanovas,[17] D. M. Castelluccio,[18,19] F. Cerutti,[6] Y. H. Chen,[8] E. Chiaveri,[6] N. Colonna,[10] G. Cortés,[17]
M. A. Cortés-Giraldo,[1] L. Cosentino,[20] L. A. Damone,[10,21] M. Diakaki,[13] M. Dietz,[22] C. Domingo-Pardo,[23] R. Dressler,[24]
E. Dupont,[13] I. Durán,[16] B. Fernández-Domínguez,[16] A. Ferrari,[6] P. Ferreira,[11] P. Finocchiaro,[20] V. Furman,[25] K. Göbel,[12]
A. R. García,[2] A. Gawlik,[7] T. Glodariu,[26] I. F. Gonçalves,[11] E. González-Romero,[2] A. Goverdovski,[27] E. Griesmayer,[9]
F. Gunsing,[6,13] H. Harada,[28] T. Heftrich,[12] S. Heinitz,[24] J. Heyse,[29] D. G. Jenkins,[30] E. Jericha,[9] F. Käppeler,[31] Y. Kadi,[6]
T. Katabuchi,[32] P. Kavrigin,[9] V. Ketlerov,[27] V. Khryachkov,[27] A. Kimura,[28] N. Kivel,[24] M. Kokkoris,[33] E. Leal-Cidoncha,[16]
C. Lederer,[22] H. Leeb,[9] S. Lo Meo,[18,19] S. J. Lonsdale,[22] R. Losito,[6] D. Macina,[6] J. Marganiec,[7] T. Martínez,[2] C. Massimi,[19,34]
P. Mastinu,[35] M. Mastromarco,[10] F. Matteucci,[36,37] E. A. Maugeri,[24] A. Mengoni,[18] P. M. Milazzo,[36] F. Mingrone,[19]
M. Mirea,[26] S. Montesano,[6] A. Musumarra,[20,38] R. Nolte,[39] A. Oprea,[26] N. Patronis,[40] A. Pavlik,[41] J. Perkowski,[7]
J. I. Porras,[6,42] J. Praena,[1,42] K. Rajeev,[43] T. Rauscher,[44,45] R. Reifarth,[12] A. Riego-Perez,[17] P. C. Rout,[43] C. Rubbia,[6]
J. A. Ryan,[14] M. Sabaté-Gilarte,[1,6] A. Saxena,[43] P. Schillebeeckx,[29] S. Schmidt,[12] D. Schumann,[24] P. Sedyshev,[25]
A. G. Smith,[14] A. Stamatopoulos,[33] G. Tagliente,[10] J. L. Tain,[23] A. Tarifeño-Saldivia,[23] L. Tassan-Got,[8] A. Tsinganis,[33]
S. Valenta,[5] G. Vannini,[19,34] V. Variale,[10] P. Vaz,[11] A. Ventura,[19] V. Vlachoudis,[6] R. Vlastou,[33] A. Wallner,[46] S. Warren,[14]
M. Weigand,[12] C. Weiss,[6,9] C. Wolf,[12] P. J. Woods,[22] T. Wright,[14] and P. Žugec[6,15]

(n_TOF Collaboration)

[1]*Dpto. Física Atómica, Molecular y Nuclear, Universidad de Sevilla, 41012 Seville, Spain*
[2]*Centro de Investigaciones Energéticas Medioambientales y Tecnológicas (CIEMAT), Spain*
[3]*Johannes Gutenberg-Universitt Mainz, 55128 Mainz, Germany*
[4]*Helmholtz-Zentrum Dresden-Rossendorf, D-01314 Dresden, Germany*
[5]*Charles University, Prague, Czech Republic*
[6]*European Organization for Nuclear Research (CERN), Switzerland*
[7]*University of Lodz, Poland*
[8]*Institut de Physique Nucléaire, CNRS-IN2P3, Univ. Paris-Sud, Université Paris-Saclay, F-91406 Orsay Cedex, France*
[9]*Technische Universität Wien, Austria*
[10]*Istituto Nazionale di Fisica Nucleare, Sezione di Bari, Italy*
[11]*Instituto Superior Técnico, Lisbon, Portugal*
[12]*Goethe University Frankfurt, Germany*
[13]*CEA Irfu, Université Paris-Saclay, F-91191 Gif-sur-Yvette, France*
[14]*University of Manchester, United Kingdom*
[15]*Department of Physics, Faculty of Science, University of Zagreb, Zagreb, Croatia*
[16]*University of Santiago de Compostela, Spain*
[17]*Universitat Politècnica de Catalunya, Spain*
[18]*Agenzia nazionale per le nuove tecnologie (ENEA), Bologna, Italy*
[19]*Istituto Nazionale di Fisica Nucleare, Sezione di Bologna, Italy*
[20]*INFN Laboratori Nazionali del Sud, Catania, Italy*
[21]*Dipartimento di Fisica, Università degli Studi di Bari, Italy*
[22]*School of Physics and Astronomy, University of Edinburgh, United Kingdom*
[23]*Instituto de Física Corpuscular, Universidad de Valencia, Spain*
[24]*Paul Scherrer Institut (PSI), Villingen, Switzerland*
[25]*Joint Institute for Nuclear Research (JINR), Dubna, Russia*
[26]*Horia Hulubei National Institute of Physics and Nuclear Engineering, Romania*
[27]*Institute of Physics and Power Engineering (IPPE), Obninsk, Russia*
[28]*Japan Atomic Energy Agency (JAEA), Tokai-mura, Japan*
[29]*European Commission, Joint Research Centre, Geel, Retieseweg 111, B-2440 Geel, Belgium*
[30]*University of York, United Kingdom*
[31]*Karlsruhe Institute of Technology, Campus North, IKP, 76021 Karlsruhe, Germany*
[32]*Tokyo Institute of Technology, Japan*
[33]*National Technical University of Athens, Greece*
[34]*Dipartimento di Fisica e Astronomia, Università di Bologna, Italy*
[35]*Istituto Nazionale di Fisica Nucleare, Sezione di Legnaro, Italy*
[36]*Istituto Nazionale di Fisica Nucleare, Sezione di Trieste, Italy*

^{37}*Dipartimento di Astronomia, Università di Trieste, Italy*
^{38}*Dipartimento di Fisica e Astronomia, Università di Catania, Italy*
^{39}*Physikalisch-Technische Bundesanstalt (PTB), Bundesallee 100, 38116 Braunschweig, Germany*
^{40}*University of Ioannina, Greece*
^{41}*University of Vienna, Faculty of Physics, Vienna, Austria*
^{42}*University of Granada, Spain*
^{43}*Bhabha Atomic Research Centre (BARC), India*
^{44}*Centre for Astrophysics Research, University of Hertfordshire, United Kingdom*
^{45}*Department of Physics, University of Basel, Switzerland*
^{46}*Australian National University, Canberra, Australia*

The spent fuel of current nuclear reactors contains fissile plutonium isotopes that can be combined with uranium to make mixed oxide (MOX) fuel. In this way the Pu from spent fuel is used in a new reactor cycle, contributing to the long-term sustainability of nuclear energy. However, an extensive use of MOX fuels, in particular in fast reactors, requires more accurate capture and fission cross sections for some Pu isotopes. In the case of ^{242}Pu there are sizable discrepancies among the existing capture cross-section measurements included in the evaluations (all from the 1970s) resulting in an uncertainty as high as 35% in the fast energy region. Moreover, postirradiation experiments evaluated with JEFF-3.1 indicate an overestimation of 14% in the capture cross section in the fast neutron energy region. In this context, the Nuclear Energy Agency (NEA) requested an accuracy of 8% in this cross section in the energy region between 500 meV and 500 keV. This paper presents a new time-of-flight capture measurement on ^{242}Pu carried out at n_TOF-EAR1 (CERN), focusing on the analysis and statistical properties of the resonance region, below 4 keV. The ^{242}Pu(n,γ) reaction on a sample containing 95(4) mg enriched to 99.959% was measured with an array of four C_6D_6 detectors and applying the total energy detection technique. The high neutron energy resolution of n_TOF-EAR1 and the good statistics accumulated have allowed us to extend the resonance analysis up to 4 keV, obtaining new individual and average resonance parameters from a capture cross section featuring a systematic uncertainty of 5%, fulfilling the request of the NEA.

I. MOTIVATION

The future of nuclear energy points to the use of innovative nuclear systems such as accelerator driven systems and Gen-IV reactors aimed at the reduction of the nuclear waste. The burned fuel from current thermal reactors can be recycled in order to separate the plutonium from the spent fuel. This plutonium contains around 66% of ^{239}Pu and ^{241}Pu (together), which are fissile and can be thus combined with natural or depleted uranium to make the mixed oxide (MOX) fuel. In this way the Pu from spent fuel and the depleted uranium, otherwise considered as waste, are used in a new reactor cycle, contributing to the long-term sustainability of nuclear energy. The use of MOX fuels has already been established on an industrial scale in thermal power reactors in several countries, but a more efficient use can be achieved in fast reactors [1].

The design and operation of these innovative systems require improved knowledge of the neutron cross sections of some of the isotopes present in the new fuel compositions such as the MOX [2]. Among the neutron cross sections that

*cguerrero4@us.es

need to be improved in terms of accuracy, the NEA Subgroup WPEC-26 [3] recommends that the capture cross section of ^{242}Pu should be measured with an accuracy of 8–10 % in the energy range between 2 keV and 500 keV (see Table I), which includes both the resolved and unresolved resonance regions.

The first attempts to measure the ^{242}Pu(n,γ) reaction were made in 1973 and 1975, when Poortmans *et al.* [4] and Hockenbury *et al.* [5] used the time-of-flight technique for measurements below 1.3 keV at the CBNM linear accelerator (Geel, Belgium) and between 6 and 87 keV at RPI (Troy, USA), respectively. A few years later, Wisshak and Käppeler [6,7] measured the cross section in the unresolved resonance region in two energy intervals, 10–90 keV and 50–250 keV. Recently, another time-of-flight measurement was carried out with the DANCE detector at LANSCE by Buckner *et al.* [8], covering the region from thermal to 40 keV but resolving resonances only up to 500 eV due to the limited neutron energy resolution of the DANCE facility. Their results, with a final systematic uncertainty around 6%, show a fairly good agreement with the evaluations in the resonance region and a systematic reduction of 20–30 % above 1 keV compared to ENDF/B-VII [9] (it is to be noted that JEFF-3.2 [10] is in agreement with ENDF/B-VII around 1 keV but 10–20 % larger at ∼10 keV).

The comparison of the measurements in the keV region shows differences of about 35%. Indeed, interpretations with the JEFF-3.1 library of the PROFIL and PROFIL-2 experiments carried out in the fast reactor PHENIX have shown an overestimation of about 14% of the ^{242}Pu integral capture cross

TABLE I. Current and required (NEA) accuracy of the ^{242}Pu(n,γ) cross section for innovative nuclear systems. ADS: accelerator driven system. SFR: sodium fast reactor.

Ref.	Nuclear device	Energy range	Accuracy (%)	
			Current	Required
HPRL [14]	(MOX fuel)	0.5 eV–2 keV	a	8
WPEC-26 [3]	ADS	9–25 keV	35	10
WPEC-26 [3]	SFR	2–500 keV	35	8

^{a}Current accuracy not stated. Improved accuracy below 2 keV is required to extract accurate individual and average resonance parameters (see text for details).

section from 1 keV–1 MeV [11–13]. Aiming at improving the evaluation of the fast energy range in terms of average parameters, the NEA, in its *Nuclear Data High Priority Request List* (HPRL) [14], requests high-resolution capture measurements with improved accuracy below 2 keV (see Table I). This should also allow us to solve the present discrepancies among average resonance parameters in the literature (see Table VII).

In order to respond to the target accuracies required by the NEA in different energy ranges, listed in Table I, a new time-of-flight measurement of the capture cross section of ^{242}Pu was proposed and approved by the CERN INTC [18] in 2013. The measurement was carried out at n_TOF-EAR1 in 2015 and preliminary results have been already presented in Refs. [19,20]. While the measurement has provided data from thermal up to at least 200 keV, this paper deals only with the analysis of the resolved resonance region, which has been extended from 1.3 keV to 4 keV. In the next section we describe briefly the n_TOF-EAR1 facility, the samples and the detection setup. The data analysis towards the capture yield is described in Sec. III. Last, the analysis of the individual resonances and their statistical properties are discussed in Secs. IV and V, respectively.

II. MEASUREMENT AT N_TOF

A. n_TOF facility at CERN

The neutron beam at n_TOF is generated through spallation of 20 GeV/c protons extracted in pulses from the CERN Proton Synchrotron and impinging on cylindrical lead target 40 cm in length and 60 cm in diameter. These pulses feature a nominal intensity of 7×10^{12} protons, delivered with a time spread of $\sigma = 7$ ns at a maximum frequency of 0.83 Hz. The resulting high-energy (MeV-GeV) spallation neutrons are partially slowed down in a surrounding water layer to produce a white neutron beam that expands in energy from thermal to a few GeV. The neutrons travel towards the two experimental areas along two beam lines: EAR1 at 185 m (horizontal) [21] and EAR2 at 19 m (vertical) [22]. Each of the experimental areas is better suited for different type of measurements depending on the specific requirements in terms of flux and resolution. While EAR1 features a better time (i.e., neutron energy) resolution, the shorter vertical beam line of EAR2 provides a poorer resolution but currently the highest instantaneous white neutron flux worldwide (see Ref. [23]),
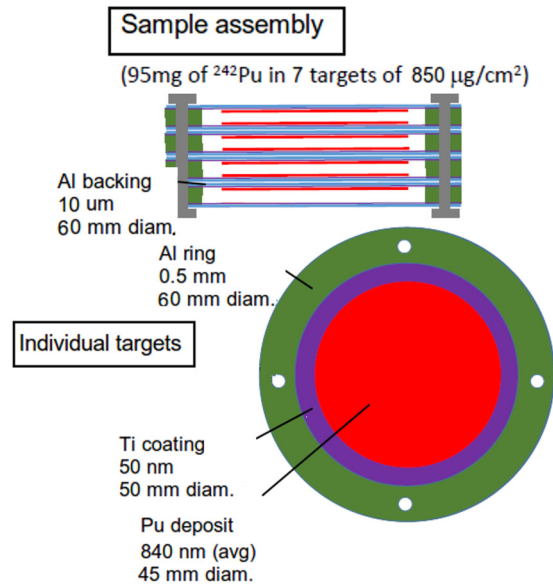

FIG. 1. Sketch of the sample assembly composed of seven thin ^{242}Pu deposits on 10 μm thick Al backings (see text for details).

which makes it especially well suited for measuring highly radioactive and/or small mass samples (see, for instance, Ref. [24]). The measurement of the ^{242}Pu(n,γ) at n_TOF, aiming at describing accurately the resonance region and not affected by a high radioactivity background, was therefore performed at EAR1.

B. ^{242}Pu and ancillary measurements

The sample preparation was carried out within the EC CHANDA project [25] by the JGU University of Mainz and the HZDR research center in Germany. The material used was 99.959% pure ^{242}Pu (main impurities: 2×10^{-4} and 2×10^{-5} of ^{240}Pu and ^{244}Pu, respectively) provided by ORNL. A set of seven thin targets 45 mm in diameter, in order to cover the complete neutron beam, were prepared by electrodeposition of 95(4) mg of ^{242}Pu on thin (10 μm) aluminum backings with a 50 nm Ti coating, resulting in targets with an average areal density of 850 μg/cm^2 of ^{242}Pu, with variations between targets within 7% (see Ref. [26] for the details). The target thickness homogeneity, studied by means of alpha radiography, was found to be 75%, leading to an overall thickness inhomogeneity of the seven targets combined below 0.1%. The assembly of seven thin targets, sketched in Fig. 1, features a total backing thickness of only 70 μm. This value is significantly smaller than in previously used actinide targets at n_TOF (see, for instance, Refs. [27–29]) and results in a reduced neutron capture and scattering associated background.

During the experiment, with a total number of 3.17×10^{18} protons (i.e., approximately one month long), most (64%) of the beam time was allocated to measure the Pu target. The background induced by the sample assembly was determined with an exact replica of the Pu target without the Pu deposits using 24% of the beam time. This replica will be called the dummy target hereafter. The background caused by the γ rays in the beam was assessed by using a lead (1 mm thick)

target that scatters photons without perturbing significantly the neutron beam. The measurement of a thick (100 μm) gold target with the same diameter as the ^{242}Pu one was used for normalization via the saturated resonance method [30], and a measurement with no target in the beam was used to estimate the background level in the lead and gold measurements. Last, measurements without beam were carried out without and with the ^{242}Pu targets in place for determining the environmental and ^{242}Pu activity backgrounds. The details about the background subtraction and normalization are given in Sec. III A.

C. Detection setup

As of today, two different detection systems are available at n_TOF for capture experiments. The full γ-ray cascade can be detected using the 4π BaF$_2$ total absorption calorimeter (TAC) [31], or just one of the γ rays of each cascade (total energy detection technique, see Sec. III B) is detected with an array of four low neutron sensitivity C$_6$D$_6$ detectors [32].

The array of four C$_6$D$_6$ was chosen for this measurement mainly because these detectors suffer significantly less from the so-called γ flash (i.e., prompt γ rays produced in the spallation reactions) than the TAC, due to their fast response and light components, thus allowing us to measure up to the maximum required neutron energy (see Table I). The setup of four detectors looking at the target from a backward position (135° with respect to the beam) in order to minimize the background from scattered in-beam γ rays is shown in the top panel of Fig. 2. The bottom panel shows the corresponding geometry implemented in the Monte Carlo simulation with

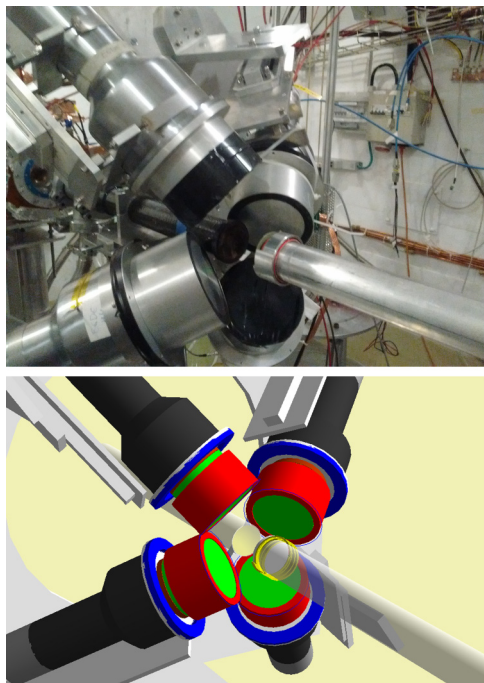FIG. 2. Top: Array of four C$_6$D$_6$ detectors used to detect the γ-ray cascades emitted following the neutron capture on the ^{242}Pu sample. Bottom: Geometry implemented in GEANT4 to simulate the response of the detection setup.

the GEANT4 toolkit [33,34] used for assessing the detection efficiency (see Sec. III B).

Two additional detectors are used at n_TOF for monitoring the proton and neutron beams. A wall current monitor (so-called PKUP) measures the intensity of the proton beam in each pulse. The neutron beam is monitored with the SiMon system [35], an array of four silicon detectors placed outside the beam and looking at a thin enriched lithium fluoride foil for detecting the products of the ^{6}Li(n,α) reaction, whose cross section is considered a standard from thermal energy to 1 MeV. The pulse-by-pulse intensities provided by these two detectors have been found to be proportional within 0.5%, which sets the accuracy in the scaling when comparing or combining different measurements, for instance for background subtraction and normalization.

Each of the detectors in the capture setup and the beam monitoring system is connected to one channel of the n_TOF Data acquisition system [36], which features 12-bit digitizers sampling at 900 MSamples/s during 100 ms following the arrival of the proton pulse to the spallation target (i.e., recording signals of reactions induced by neutrons for energies down to 18 meV). The full data movies are automatically transferred from the DAQ computers to the CERN Advanced Storage manager (CASTOR) for their long-term storage and off-line analysis.

III. ANALYSIS

A. Data reduction

The digitized signals recorded by the n_TOF DAQ and stored in CASTOR are analyzed using the pulse shape analysis routine described in Ref. [37]. In particular, the C$_6$D$_6$ signals are analyzed by comparing each of them with reference pulse shapes characteristic of each detector (see Refs. [37,38] for details). The amplitude, area and time-of-flight of each identified detector signal are stored together with the information on the proton pulse (date, time, type, and intensity). The corresponding neutron energy is then calculated using the nonrelativistic formula:

$$E_n = \frac{1}{2} m_n \left(\frac{L_0 + \lambda(E_n)}{t - t_0} \right)^2, \tag{1}$$

where m_n is the neutron mass, L_0 is the flight path from the target exit to the experimental area, t is the signal time, t_0 is the start time (calculated from the arrival of the γ flash to each detector), and $\lambda(E_n)$ is an energy-dependent equivalent moderation length, related to the resolution function of the facility. The neutron energy dependence of λ reflects the fact that neutrons of a given energy are not produced instantaneously with the arrival of the proton beam but take some time to be produced, moderated, and transported outside the spallation target assembly (see Ref. [39] for a more detailed explanation).

Accurate amplitude-to-energy calibrations and gain stability checks for the four C$_6$D$_6$ detectors were performed on a weekly basis using ^{137}Cs, ^{88}Y, ^{241}Am/^{9}Be, and ^{244}Cm/^{13}C calibration sources. The small time-dependent gain shifts observed were corrected for and, as a result, the weighted (defined in Sec. III B) counting rates remained constant within 0.5% along the full length of the experiment (one month).
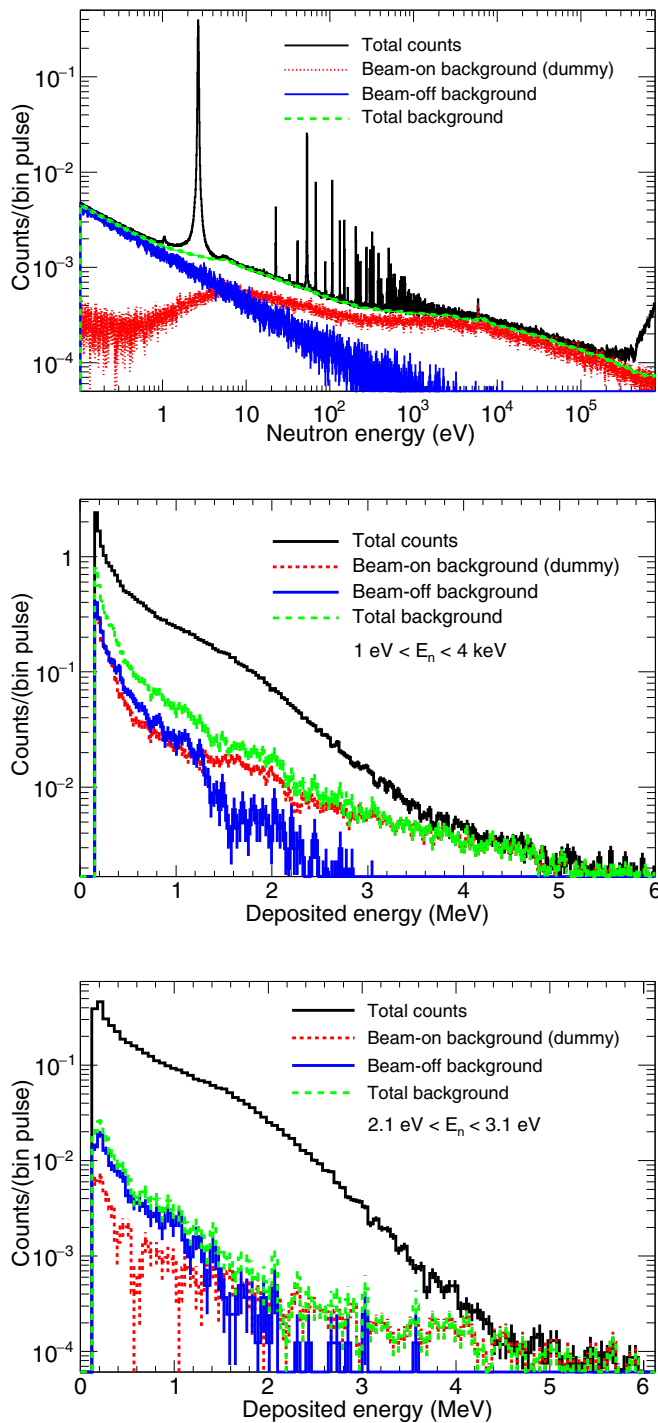
FIG. 3. Unweighted counting rates per pulse for the ^{242}Pu and background measurements as a function of the neutron energy in the full energy range measured at n_TOF-EAR1 (top). Energy deposition in the C_6D_6 detectors corresponding to the full neutron energy range analyzed in this paper (1 eV–4 keV) (middle) and with neutron energy cuts to select just the largest resonance (2.67 eV) (bottom).

The measured counting rates as a function of neutron energy (with energy deposited in the detectors E_{dep} larger than 150 keV) are displayed in the top panel of Fig. 3, where it is observed that the beam-off background (constant in time)

dominates only below 10 eV. The beam-dependent background (dotted red line), determined with the measurement of the dummy target, is the major contribution to the counting rate at higher energies. The dashed green (light gray) curve in this figure shows the level of the overall background, in which the in-beam γ-ray background is also included. The latter, although strongly suppressed due to the inclusion of ^{10}B in the moderator (see Ref. [21]), is still a relevant source of background especially in the unresolved resonance region [19]. Last, the counting rate increases at neutron energies above 306 keV. This is related to the opening of the first inelastic channel above the γ-ray energy detection threshold.

The middle and bottom panels of Fig. 3 show the measured counting rates as a function of the deposited γ-ray energy. While the middle panel contains data for all the neutron energy range under study, the bottom panel corresponds just to neutron energies inside the first capture resonance (2.1–3.3 eV). The latter hence shows an enhanced capture to background ratio compared to the detector response integrated over the full neutron energy range of the resonance region. The spectra of deposited energy indicate that the beam-off, i.e., the room and ^{242}Pu sample activity background are mainly low energy γ rays while the high-energy γ-ray background is related to the beam (dummy).

Besides neutron capture, two additional neutron-induced reactions in ^{242}Pu can contribute to the measured counting rate: neutron scattering and fission. Considering the elastic scattering, the cross section is 10–100 times larger than capture but the C_6D_6 detectors have a negligible neutron sensitivity (4 orders of magnitude below the efficiency for capture). Therefore, the neutron scattering contribution has been considered negligible. As for the fission, the efficiency of the detection array is slightly larger than for capture due to the larger γ-ray multiplicity. However, it is also considered negligible since the fission cross section in the energy range of interest remains on average 3 orders of magnitude below the one of capture with the exception of few resonances excluded from the resonance analysis (see Sec. IV),

B. Total energy detection technique

The detection efficiency depends, in general, on the cascade pattern (i.e., the γ-ray energies and multiplicities). To avoid this dependency, neutron capture measurements with C_6D_6 detectors are analyzed following the total energy detection (TED) technique [40,41]. This is based on two principles:

(i) The efficiency of the detectors must be low enough so that at most one γ ray per cascade is detected. The total efficiency for detecting a cascade ε_c becomes

$$\varepsilon_c = 1 - \prod_i (1 - \varepsilon_i) \approx \sum_i \varepsilon_i, \qquad (2)$$

ε_i being the efficiency to detect a γ ray of the cascade. The sum goes over all emitted gammas i.

(ii) The efficiency to detect each γ ray is proportional to its energy E_i ($\varepsilon_i = k \cdot E_i$), hence:

$$\varepsilon_c = k \sum_i E_i = k \cdot E_c. \qquad (3)$$

Under these two conditions the efficiency for detecting a cascade is proportional to the known energy of the cascade (E_c) and independent of the actual decay path. However, the second requirement is not fulfilled by C_6D_6 detectors and therefore a mathematical manipulation of the detector response is needed to achieve the proportionality between detection efficiency and γ-ray energy: the counts recorded at each deposited energy are weighted by a factor dependent on its energy (pulse height), given by the so-called weighting function (WF). This is known as the pulse height weighting technique (PHWT) [41].

Following the prescription from Ref. [41], the WF for each sample (^{242}Pu and ^{197}Au) has been calculated from the detector response to monoenergetic γ rays from 50 keV–10 MeV obtained via Monte Carlo simulations of the detection system carried out with a GEANT4 application developed for this purpose [42]. The very detailed geometry implemented in GEANT4, displayed in Fig. 2, includes even details of the Pu target assembly in order to consider, among other effects, the attenuation of photons in the ^{242}Pu targets and backings as well as the neutron self-shielding for the largest resonances. The resulting WFs, calculated to have a proportionality constant $k = 1$ in Eq. (3), are third- to fourth-degree polynomials (depending on the sample). The application of these WFs to the response of the detectors allows satisfying the proportionality condition $\varepsilon_i = k \cdot E_i$ within 1% for all the simulated γ-ray energies between 0.1 and 10 MeV. The corrections and systematic uncertainties associated to this technique are discussed in the following section.

C. Corrections to the detection efficiency

The application of the PHWT results in a detection efficiency numerically equal to the energy of the capture cascade [Eq. (3) with $k = 1$]. This is in principle independent of the decay pattern, but there are actually some effects and corrections to be considered:

(i) the possible detection of more than one γ ray (multiple counting) from a cascade in our detection setup, f_{mc};

(ii) the counts lost below the detection threshold in γ-ray energy, f_{thr}; and

(iii) the probability of internal conversion leading to the emission of nondetectable electrons instead of γ rays, f_{ce}.

The associated corrections f_{mc}, f_{thr}, and f_{ce} are calculated with the help of Monte Carlo simulations of the detection system response to capture cascades. The cascade generator CAPTUGENS [43] was used to generate realistic cascades emitted by the compound nuclei ^{243}Pu and ^{198}Au at an excitation energy S_n, considering in both cases a completely known level scheme, γ-ray transition probabilities, and internal conversion factors (all from ENSDF [44]) below a certain excitation energy E_{cut} (400 keV for ^{243}Pu and 1600 keV for ^{198}Au), and then a statistical model (based on level density parameters and photon strength functions) to generate transitions starting above E_{cut}. The statistical parameters were taken from Refs. [45] and [46] for ^{198}Au and ^{243}Pu, respectively. The generated cascades were coupled to the GEANT4 application developed to simulate the detector response for the PHWT, resulting in the good
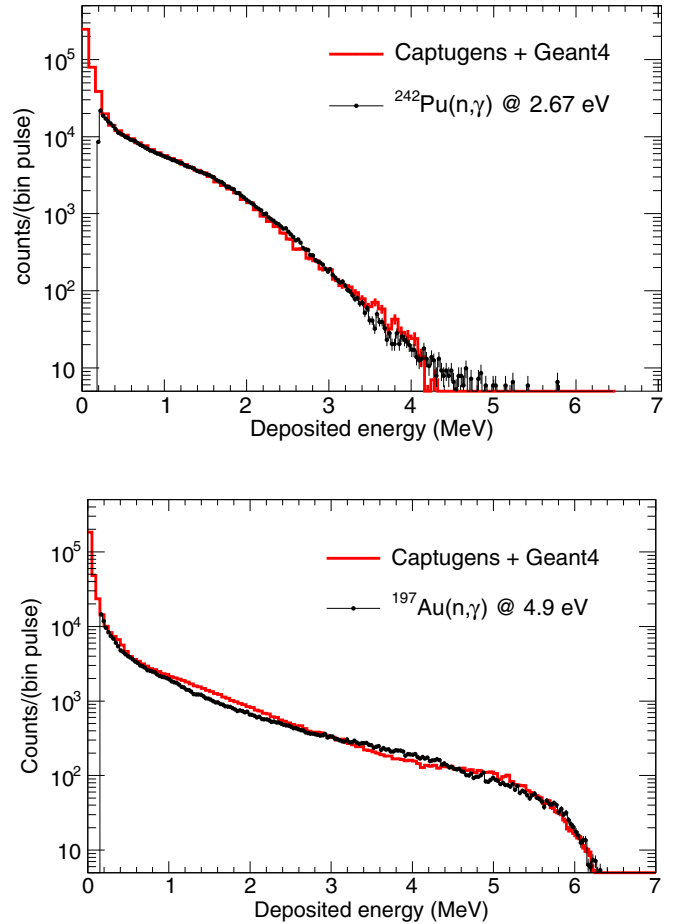

FIG. 4. Top: Energy deposited spectrum in the C_6D_6 in the 2.67 eV ^{242}Pu(n,γ) resonance compared to the simulated response. Bottom: Experimental response compared to the simulated one for the 4.9 eV resonance of ^{197}Au(n,γ) cross section. The low-energy fraction missing in the experimental spectra f_{thr} is corrected according to the simulations.

agreement between the experimental and simulated responses shown in Fig. 4 for both ^{242}Pu(n,γ) and ^{197}Au(n,γ) cascades.

The correction factors are calculated by comparing the efficiency from the simulation of cascades when each of these effects is included with respect to the expected value $\varepsilon_c = E_c$, given by Eq. (3) with $k = 1$. The f_{mc} correction, below 0.5%, is already applied during the analysis by considering only one of the simultaneously detected γ rays (i.e., belonging to the same capture cascade). f_{thr} and f_{ce} have been calculated for several detection thresholds, showing that f_{ce} is at most 0.4% for the minimum threshold of 150 keV applied in the subsequent analysis. Therefore only f_{thr} is sizable and quite different for each isotope, ranging up to 15% and 8% for ^{242}Pu(n,γ) and ^{197}Au(n,γ), respectively, for energy thresholds smaller than 250 keV. In order to keep this correction small, a threshold of 150 keV was used for the analysis. The values of correction factors obtained and their associated uncertainties are summarized in Table II.

The validation of these corrections is assessed by comparing the corresponding corrected counting rates for different energy

TABLE II. Yield correction factors related to the deviations from the PHWT theory, being just f_{thr} sizable with the actual experimental conditions. The uncertainties in the table are derived from the statistics in the simulations.

E_{thr}	f_{thr}			f_{ce}	f_{mc}
	250 keV	200 keV	150 keV	150 keV	
^{242}Pu	1.150(4)	1.121(4)	1.090(3)	1.004(3)	0.995(3)
^{197}Au	1.078(3)	1.066(3)	1.052(3)	1.001(3)	0.998(3)
^{242}Pu/^{197}Au	1.067(4)	1.052(4)	1.035(4)		

thresholds. The results for thresholds between 150 and 250 keV agree within 0.2% and 1% for ^{197}Au(n,γ) and ^{242}Pu(n,γ), respectively. Therefore, a systematic uncertainty of 1.5% has been estimated for these corrections. Additionally, the simulated cascades allow to estimate the deviation from the PHWT theory given by Eq. (3) related to the performance of the weighting functions. The deviation is found to be within 0.5% for both the ^{242}Pu and Au samples and this value is considered as the associated uncertainty.

D. Capture yield

The neutron capture yield is the probability for an incident neutron to undergo a capture reaction and is related to the capture σ_{γ} and total σ_{tot} cross sections as:

$$Y(E_n) = (1 - e^{-n\sigma_{tot}})\frac{\sigma_{\gamma}}{\sigma_{tot}},\qquad(4)$$

where n represent the sample's areal density. Under the thin target approximation $n\sigma_{tot} \ll 1$, which applies in this measurement with the exception of the largest resonance, the capture cross section can be directly extracted from the experimentally obtained capture yield $Y = n\sigma_{\gamma}$. The latter is calculated as:

$$Y(E_n) = \frac{f_{mc}f_{thr}f_{ce}}{f_{SRM}} \cdot \frac{C_w(E_n) - B_w(E_n)}{\Phi(E_n) \cdot \varepsilon_c},\qquad(5)$$

C_w and B_w being the weighted distributions of total and background counts per pulse obtained from the measured counting rates displayed in Fig. 3, $\Phi(E_n)$ the total number of neutrons of a given energy E_n reaching n_TOF-EAR1 in each pulse [47], ε_c the detection efficiency [see Eq. (3)] and f_{mc}, f_{thr}, and f_{ce} the correction factors to the efficiency discussed in the previous section. Last, f_{SRM} is the absolute normalization factor obtained via the saturated resonance method (SRM) [30] using the first (4.9 eV) resonance of ^{197}Au. The 100 μm thickness of the gold target is such that this resonance saturates, i.e., almost all neutrons undergo at least one interaction, and this saturation level provides the means to normalize the ^{242}Pu capture yield. The saturated resonance of ^{197}Au has been fitted for each detector to extract individual normalization factors f_{SRM}, as listed in Table III. Figure 5 shows the fit of this resonance in the average yield of the four detectors using the SAMMY code [48].

The deviations in f_{SRM} between the individual detectors are related mainly to uncertainties in the efficiency and in the positioning (distance and angle) of the detectors with respect to the target. Both effects affect equally to the ^{197}Au and ^{242}Pu

TABLE III. Normalization factors f_{SRM} obtained for each detector from the fit of the ^{197}Au(n,γ) 4.9 eV saturated resonance using the SAMMY code. The right column presents the ratios of the individual normalized ^{242}Pu 2.67 eV resonance kernels, Y_{norm}, with respect to the average value of the four detectors, $\langle Y_{norm} \rangle$. The uncertainties in the table are due the uncertainty in the fit of the saturated resonance and the counting statistics.

	f_{SRM} ($E_{thr} = 150$ keV)	$Y_{norm}/\langle Y_{norm} \rangle$
C_6D_6-1	0.853(3)	1.012(4)
C_6D_6-2	0.994(3)	1.003(4)
C_6D_6-3	0.891(3)	0.990(4)
C_6D_6-4	0.914(3)	0.995(4)
All C_6D_6	0.914(2)	

measurements and therefore cancel out with this normalization method. A verification of the correctness of the individual f_{SRM} comes from the fact that the 2.67 eV resonance kernels in the normalized ^{242}Pu yields from individual detectors agree with the average within about 1%, as presented in Table III.

The systematic uncertainties from different sources contributing to the resulting yield are summarized in Table IV. The uncertainty related to the relative positioning along the beam line of the ^{197}Au and ^{242}Pu samples is assumed to be ± 1 mm, leading to a 1.5% additional uncertainty in the normalization. Table IV also includes the energy-dependent uncertainty of the neutron flux shape, 1% below 100 eV and 2% at higher energies [47]. It is to be noted that the uncertainty in the background subtraction is considered negligible because it does not affect the analysis of individual resonances. The resulting quadratic sum of partial systematic uncertainties in the ^{242}Pu yield is 3.2% or smaller. An additional uncertainty of 4% related to the determination of the sample mass has to be considered
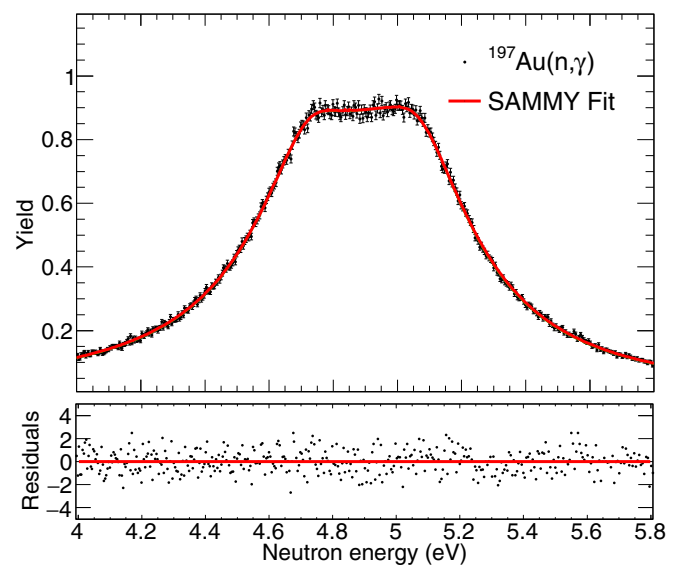

FIG. 5. Saturated resonance at 4.9 eV in the experimental capture yield of ^{197}Au fitted with the SAMMY code. The average of the four detectors is shown.

TABLE IV. Summary of the estimated individual systematic uncertainties contributing to the final uncertainty in the ^{242}Pu capture yield grouped according to their origin. The uncertainty in the sample mass contributes additionally in the extraction of the cross section from the capture yield. The upper limit in the total systematic uncertainties corresponds to the energy range 100 eV < E_n < 4 keV.

General group	Partial origin	Syst. unc. (%)
Neutron flux	Flux shape (E_n < 100 eV)	1
	Flux shape (100 eV < E_n < 4 keV)	2
Efficiency (PHWT)	Efficiency correction factors	1.5
	Deviation PHWT theory	0.5
	Gain shift	0.5
Normalization	Deviation yields individual detectors	1
	Relative position Au/Pu	1.5
	Beam monitors	0.5
	Sample mass	4
	Total (capture yield)	<3.2
	Total (cross section)	<5.1

in the subsequent extraction of the capture cross section. The resulting systematic uncertainty in the cross section is 5.1% or smaller, clearly lower than the 8% required by the NEA for the design and operation of advanced nuclear devices (see Table I).

One last consideration in the calculation of the yield is related to the statistical fluctuations. The capture yield obtained using the prescription of the PHWT shows enhanced statistical fluctuations, especially in the resonances with few counts, with respect to those related to counting statistics. These enhanced fluctuations, inherent in the PHWT method, limit the maximum energy of analyzable resonances. In order to expand the energy range in the subsequent resonance analysis, we have verified that for ^{242}Pu (may be true for heavy 0^+ nuclei, in general), the cascade spectrum is the same independently of the neutron energy. Thus, the unweighted yield scaled with the appropriate average weighting factor, which accounts for the efficiency and the associated corrections described in this section, is perfectly compatible within the uncertainties with the one extracted following the usual PHWT method. Given all of the above, the unweighted scaled yield has been chosen for the analysis in Sec. IV.

IV. RESONANCE ANALYSIS

A. Individual resonance parameters

Once the capture yield has been obtained, the resonance analysis is performed using the SAMMY code [48], which allows fitting experimental time-of-flight data using the Reich-Moore approximation to the R-matrix theory. The code features different models to consider experimental effects such as self-shielding, multiple scattering, residual background, and Doppler and resolution broadenings.

A total of 251 resonances have been observed and analyzed between 1 eV and 4 keV, leaving out of our analysis the few resonances where fission contributes significantly (see Table VIII). In order to extract the individual resonance parameters, first the spin of all resonances have been set to $J = 1/2$
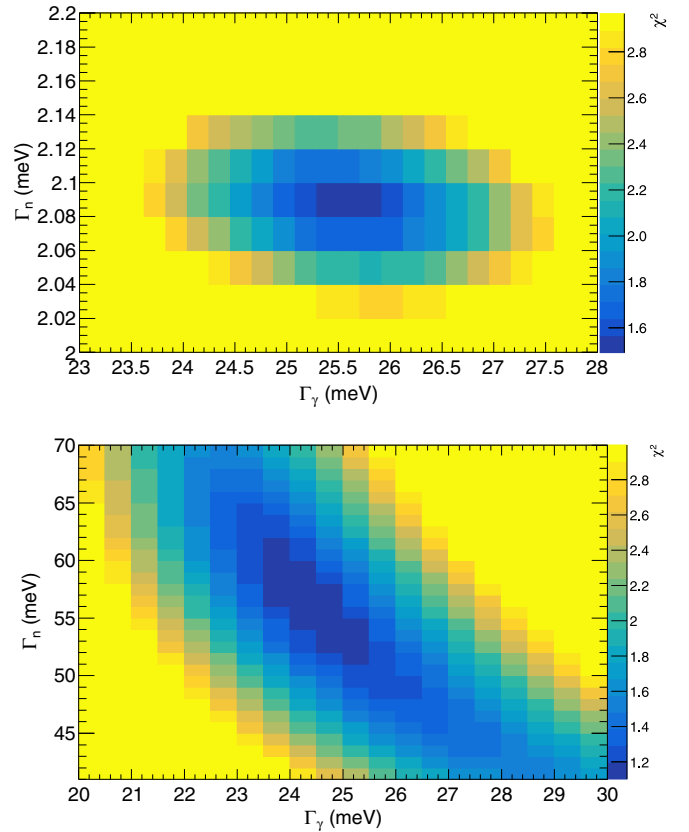

FIG. 6. Two-dimensional (2D) plots showing the evolution of the reduced χ^2 of the fit (color scale) as a function of the Γ_n-Γ_γ values for the 2.67 eV (top) and 53.5 eV (bottom) resonances.

(assumed to be s-waves) since ^{242}Pu is an even-even target. Then, the fission widths have been fixed to the values measured by Auchampaugh *et al.* [49] or Weigmann *et al.* [50], assuming a value of 0.01 meV for the rest, as recommended in JEFF-3.2 (see Table VIII). The radiative capture width is expected to be a constant (actually, it is expected from statistical model to fluctuate around the average value with a rms of about ∼3% [51]). In order to determine the value of $\langle\Gamma_\gamma\rangle$, a systematic study of the χ^2 of the SAMMY calculations (experimental cature yield vs. parameterized yield as a function of Γ_γ and Γ_n) was carried out among the largest resonances below 1.5 keV, using those showing a well-bound Γ_γ around the minimum χ^2 to compute the average Γ_γ. The average value $\langle\Gamma_\gamma\rangle$ resulting from this analysis has been used as a fixed parameter for the analysis of all the other resonances, where the only free parameters are the resonance energy and neutron width. An example of the mentioned distributions of the reduced χ^2 (i.e., χ^2 over the number of experimental points) as a function of the radiative and neutron width values is given in Fig. 6 for the two largest resonances, both showing a well-bound minimum. While this method worked for the majority of the fitted resonances, some SAMMY fits of resonances with $\Gamma_n \gg \Gamma_\gamma$, featuring a very low sensitivity to Γ_n in the fit, converged after many iterations towards too large Γ_n values, inconsistent with the evaluated resonance parameters extracted from a multichannel analysis of all available measurements. For those cases, the Γ_n was
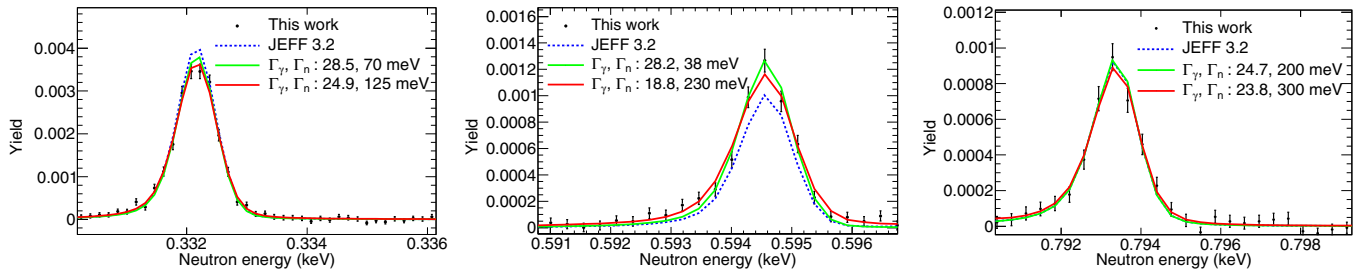
FIG. 7. Example of the sensitivity of resulting SAMMY fits to different combination of Γ_n and Γ_γ showing the compatibility of the fit with overestimated Γ_n (red/dark gray) compared to the fit with a Γ_n value consistent with evaluations (green/light gray). JEFF-3.2 is also shown as a reference (dotted blue line).

bound to a smaller value consistent with the evaluations and then the Γ_γ was fitted. Figure 7 shows the most extreme cases where one can see that a large reduction in Γ_n does not compromise the quality of the fit. The difficulties to adjust Γ_n on capture data are due to the absence of transmission data with the same sample to constrain the value of Γ_n in the SAMMY calculation.

Regarding the Doppler model used in the calculations with SAMMY, this plays a role only at low energies. Indeed, the analysis of the lowest-energy resonance with the commonly employed free gas model (FGM) is not satisfactory, giving, for instance, a reduced χ^2 of 4.7. The use of the more realistic crystal lattice model (CLM), in this case with a uranium oxide phonon description (SAMMY example file 124d), results in a better fit, as shown in Fig. 8, with a reduced χ^2 of only 1.9. Regarding the second largest resonance, at 53.5 eV, the fits are excellent with both models and the extracted radiative kernels agree within 0.1%. Therefore the resonances at higher energies were all analyzed using the FGM, since the difference with
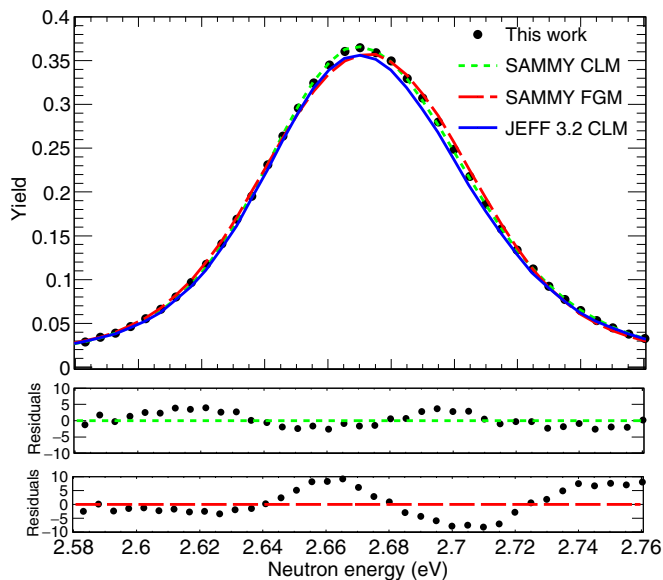
respect to the results with the CLM are negligible but the computing time is significantly reduced.

The resulting list of individual resonance parameters and radiative kernels up to 4 keV is presented in Table VIII of Appendix. In this table several resonances are marked as possible p waves. The criterion for marking possible p-wave resonances is based on the probability of occurrence of p-wave resonances (see next section). Figure 9 shows several energy ranges of the measured capture yield below 1.3 keV together with the corresponding SAMMY fit and the yields corresponding to the ENDF/B-VII [9] and JEFF-3.2 [10] evaluated cross sections.

The good neutron energy resolution of n_TOF-EAR1 combined with the high statistics of the new capture data have allowed us to extend the resolved resonance region up to 4 keV, which is significantly higher than the current limit in the evaluations, which are based on the resonance parameters reported in Refs. [4,49,50]. This extension is illustrated in Figs. 9–10, showing SAMMY fits from just above the current 920 eV and 1.3 keV energy limit for resonance parameters in ENDF/B-VII.1 [9] and JEFF-3.2 [10], respectively, up to 4 keV. In the resonance analysis above 1.3 keV, the energies and neutron widths in Refs. [49,50] were used as initial parameters for the fit and to help identifying small resonances.

B. Comparison to evaluated cross sections

The different resonances displayed in Fig. 9 are illustrative examples of resonances currently present in the evaluations that can be confirmed (75) or rejected (7) according to the new capture data. For instance, we confirm the presence of a doublet at 504 eV, as already suggested by Poortmans *et al.* [4], but we do not see the resonance at 14 eV listed in evaluations, confirming what Buckner *et al.* reported [8]. In addition, 19 new resonances have been identified within JEFF-3.2's resonance region (some examples in Fig. 9). Since these new resonances are usually weak, some of them are most likely p-wave resonances, as it is discussed in Sec. V.

The quantitative cross-section comparison between the results of this work and of JEFF-3.2 is made in terms of radiative kernel (R_K), calculated from the resonance parameters as:

$$R_K = g_J \frac{\Gamma_\gamma \Gamma_n}{\Gamma_\gamma + \Gamma_n + \Gamma_f}, \qquad (6)$$

FIG. 8. SAMMY fits and residuals of the largest ^{242}Pu capture resonance using free gas (FGM) and a crystal lattice (CLM) models to describe the Doppler broadening. The fit obtained using the resonance parameters in JEFF-3.2 or ENDF/B-VII.1 (CLM) is shown as a reference.
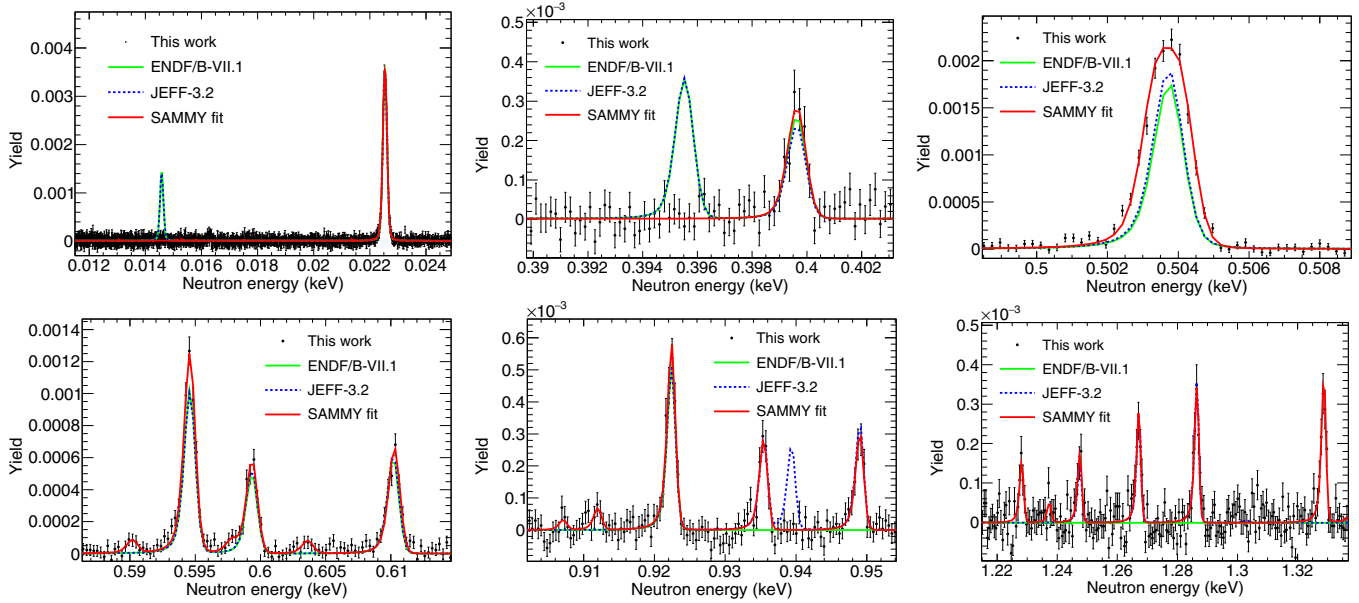
FIG. 9. Capture yield from n_TOF together with the SAMMY fit (red/dark gray line) and the predictions from JEFF-3.2 (dashed line) and ENDF/B-VII.1 (green/light gray line) in several neutron energy ranges below 1.3 keV where significant differences are found.

with the spin factor g_J defined as $g_J = \frac{(2J+1)}{(2I+1)(2i+1)}$, where $J, I = 0$ and $i = 0.5$ are the spins of the resonance, target nucleus, and neutron, respectively. Radiative kernels (R_K) have been compared individually for each resonance and integrated over 200 eV energy intervals. The R_K of each resonance is listed in Appendix together with the ratio of n_TOF with respect to the $R_K S$ calculated from the resonance parameters in JEFF-3.2 and in the recent measurement at DANCE [8]. The listed R_K ratios have been studied as a function of the fission, scattering, and capture widths in order to look for correlations that could hint at systematic errors or biases, but no correlations have been found.

The top panel of Fig. 11 shows the individual ratios of n_TOF $R_K S$ (this work) with respect to JEFF-3.2 (72 common resonances). This comparison stops at 1300 eV, since no resonance parameters are included in the evaluations above this energy. For an overall comparison, the individual $R_K S$ have been grouped over 200 eV energy intervals for n_TOF and JEFF-3.2. The ratio of the integrated R_K (i.e., cross section) in each energy interval is shown with a red line in the top panel of Fig. 11, where the shadowed area corresponds to the statistical uncertainty of the sum of $R_K S$ in each range. A minimum integral ratio n_TOF/JEFF of 1.028(5) is found below 200 eV, while average differences larger than 12% are observed in the

FIG. 10. The capture yield in this work fitted using the SAMMY code in different energy ranges from 1 to 4 keV.

FIG. 11. Top: Ratio of individual radiative kernels obtained in this work with respect to JEFF-3.2 (black) as a function of the neutron energy together with the weighted mean (dashed blue line). The solid red line coresponds to the ratio of the integrated R_K over 200 eV intervals and the shadowed area illustrates the statistical uncertainty of the R_K integral in each energy interval. Bottom: Ratio of individual R_K in this work to JEFF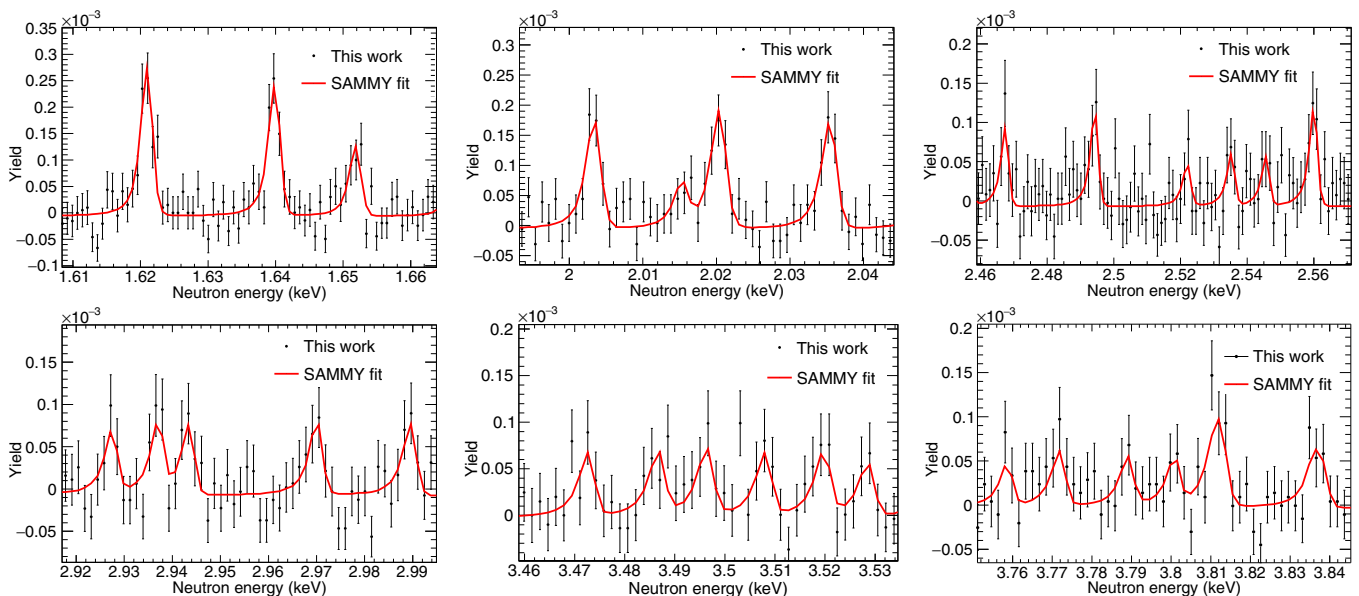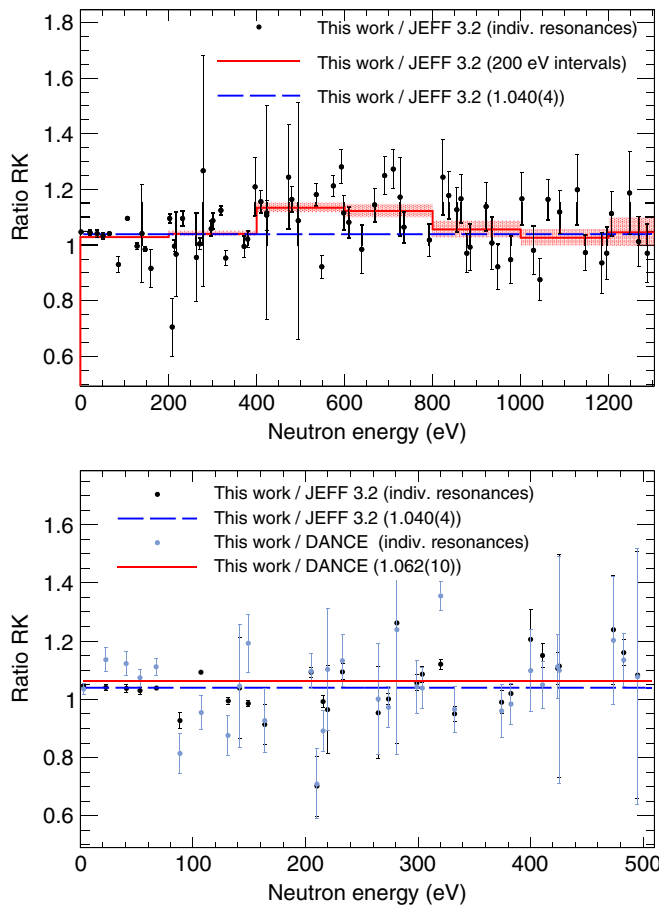-3.2 and DANCE below 500 eV together with their weighted means (dashed and solid line, respectively). The values in brackets in the legend correspond to the weighted mean of the ratios.

400–800 eV region and compatible results within the statistical uncertainty are obtained above 1 keV.

The bottom panel of Fig. 11 zooms in on the first 500 eV and includes the ratio of individual $R_K S$ in this work with respect to the recent measurement in DANCE (35 common resonances). Overall, the n_TOF data suggest that the $R_K S$ are on average 4.0 (4)% higher than JEFF-3.2 and 6.2 (10)% higher than DANCE, in terms of weighted mean (weighted on radiative kernel). The comparison of the measured and evaluated R_K for the largest ^{242}Pu resonance, at 2.67 eV, indicates that the new value is 4.2 (2)% larger than the one in JEFF-3.2 (or ENDF-VII.1). For the same resonance, according to Ref. [8], DANCE reports a resonance integral larger than the evaluations by 2.4%.

The 4% higher cross section found in this work below 1 keV with respect to the evaluations does not compromise the suggested [11–13] reduction of 14% in the integral cross section between 1 keV and 1 MeV because the evaluations

are based on completely different data sets below and above 1.3 keV. In the resonance region, the resonance widths and energies are taken from Refs. [4,49,50], while the unresolved resonance region is based in the 40-year-old measurements of Refs. [5–7] between 6 and 210 keV. The analysis of the unresolved resonance region from the n_TOF experiment described herein will be presented and compared with the evaluations, those data and the recent measurement at DANCE [8] in a forthcoming work aimed at shedding some light on the possible overestimation of 14% in the high-energy evaluated capture cross section of ^{242}Pu.

V. STATISTICAL PROPERTIES OF RESONANCE PARAMETERS

Average resonance parameters of s-wave resonances—specifically, the average resonance radiative width, $\langle\Gamma_\gamma\rangle$, neutron strength function, S_0, and the average resonance spacing, D_0—can be obtained from the individual resonance parameters in Table VIII.

A. Average radiative width

Total radiative widths are given by the sum of partial radiation widths to all levels below the neutron separation energy S_n. Individual partial radiation widths from different neutron resonances to a fixed level are expected to fluctuate according to the Porter-Thomas distribution around the expectation value. The huge number of available final levels makes the distribution of radiation widths significantly narrower than the Porter-Thomas distribution, especially for heavy nuclei. Statistical model calculations of total radiative widths for ^{242}Pu, carried out using the constant-temperature level density model, indicate that the individual Γ_γ values of s-wave resonances should fluctuate within 3–3.5 % around $\langle\Gamma_\gamma\rangle$. The average total radiative width $\langle\Gamma_\gamma\rangle$ has been obtained from 27 resonances for which both Γ_γ and Γ_n were fitted (Γ_γ values with uncertainties in Table VIII), following the steps explained at the end of Sec. IV A. This set of total radiation widths is shown in Fig. 12 with its weighted average, where the dark and light shadowed regions correspond to the uncertainty of the average value and the standard deviation of the weighted distribution of Γ_γ values, respectively. The value $\langle\Gamma_\gamma\rangle = 24.8(5)$ meV, is recommended according to our analysis. Our expectation result is higher than the expectation values in the literature, summarized in Table VII and significantly larger than the value in ENDF/B-VII.1.

B. Strength function

The estimate of the s-wave neutron strength function S_0 can be calculated from the distribution of reduced neutron widths $\Gamma_0 = \Gamma_n/(E_n)^{1/2}$ in a given energy range ΔE_n as follows

$$S_0 = \frac{1}{\Delta E_n}\Sigma_i g_J \Gamma_{0,i}, \qquad (7)$$

Besides the statistical uncertainty in Γ_0 (errors bars in Fig. 13), the uncertainty in S_0, labeled as ΔS_0, is based on the variation of the sum of neutron widths distributed in accordance with
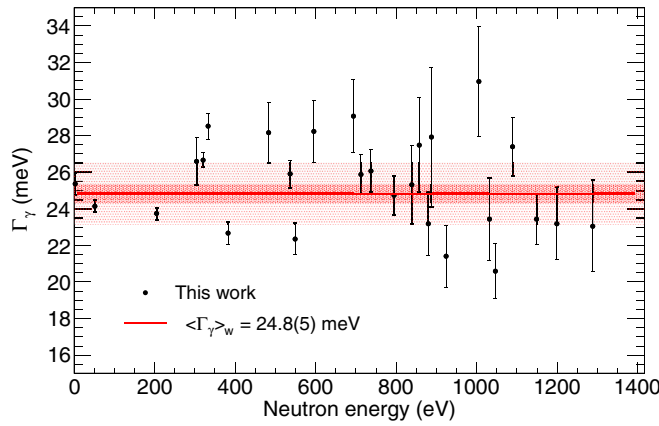
FIG. 12. Experimental values of *Gamma*$_\gamma$ for individual resonances are shown together with the average total radiative width. The narrow shadowed region indicates the uncertainty in $\langle \Gamma_\gamma \rangle$ and the broader one shows the one standard deviation corridor around the obtained average.

the Porter-Thomas law [52] and is commonly calculated as

$$\frac{\Delta S_0}{S_0} = \sqrt{\frac{1}{N_0}\left(\frac{4}{\pi} + 1\right)}, \tag{8}$$

being N_0 the total number of resonances considered in the sum.

The cumulative distribution of experimental widths is shown in Fig. 13. This figure shows the compatibility of this work within the statistical uncertainty with the S_0 of previous measurements up to 1300 eV compiled in JEFF-3.2. Individual widths Γ_0 were summed in different energy ranges up to 4000 eV to extract the average neutron strengths. The results are presented in Table V, showing consistent values of S_0 within 1σ for all the studied energy intervals. The uncertainties in brackets in Table V, calculated using Eq. (8), are larger than the ones from the sum of reduced neutron widths $\sigma(\Sigma_i g_J \Gamma_{0,i})$. The value obtained in the full energy
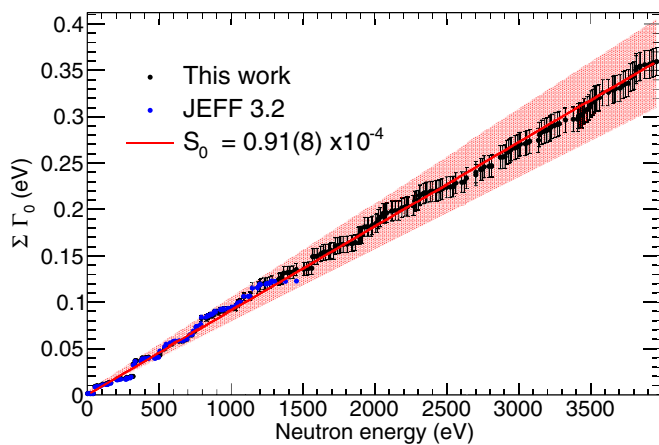

FIG. 13. Sum of the reduced neutron widths Γ_0 as a function of the neutron energy in this work compared to JEFF-3.2. The red line shows nice consistency of the obtained value for S_0 in the full energy range up to 4 keV. The total uncertainty of S_0 is shown as a shadowed area.

TABLE V. Neutron strength function S_0 in different energy intervals and the full energy range up to 4000 eV. $\sigma(\Sigma_i g_J \Gamma_{0,i})$ is the uncertainty in S_0 from the sum of reduced neutron widths. The right column shows the deviation of the individual strength in each interval with respect to the value extracted in the full range.

E_n (eV)	$10^4 \times S_0$	$\sigma(\Sigma_i g_J \Gamma_{0,i})$	Deviation (σ)
0–500	0.84×(20)	0.02	−0.78
500–1000	1.01×(25)	0.06	1.09
1000–1500	0.9(3)	0.12	−0.48
1500–2000	0.95(24)	0.15	0.51
2000–2500	0.82(21)	0.10	−0.95
2500–3000	0.9(3)	0.13	−0.38
3000–3500	0.84(25)	0.10	−0.73
3500–4000	1.0(3)	0.12	0.94
0–4000	0.91(8)	0.04	

range, $S_0 = 0.91(8)10^{-4}$, has a reduced uncertainty compared to previous experimental values (see, for instance, Ref. [4]) due to the much larger number of observed resonances. The value of S_0 obtained is slightly smaller but still compatible with the ones provided by JEFF-3.2 (1.0010^{-4}) and ENDF/B-VII.1 (1.0210^{-4}) and supports the reduction of S_0 proposed by Rich *et al.* [$0.91(20)10^{-4}$].

In the energy range above 3.7 keV, the S_0 was found to be strongly dependent on two resonances. First, the resonance at around 3840 eV could not be fitted using a value of Γ_n compatible with the overall S_0 value from lower energies unless a doublet was included. Following the same consistency criterion, the neutron width of the resonance at 3728 eV, with a very large value reported in Ref. [49], was set to 200(180) meV since the SAMMY calculation did not converge to a unique value due to the scarce statistics. Removing this resonance would affect the extracted value of S_0 less than 1% and even if the full energy range above 3700 eV is discarded the value of S_0 obtained from 0–3700 eV would be just 1.7% smaller than the $S_0 = 0.91 \times 10^{-4}$ suggested from this analysis.

Last, the obtained S_0 is not affected by possible missing s-wave resonances or misidentified p waves since they represent a negligible fraction of the resonance strength.

C. Average level spacing

The average level spacing D_0 is usually estimated from the cumulative number of observed resonances N_0 in an interval of neutron energies ΔE_n:

$$D_0 = \frac{\Delta E_n}{N_0}. \tag{9}$$

The statistical uncertainty ΔD_0, assuming the Wigner law [53] for the distribution of the next neighbor level spacings, is given by

$$\frac{\Delta D_0}{D_0} = \sqrt{\frac{1}{N_0}\left(\frac{4}{\pi} - 1\right)}. \tag{10}$$

The cumulative plot of the number of observed resonances as a function of the neutron energy is presented in Fig. 14.
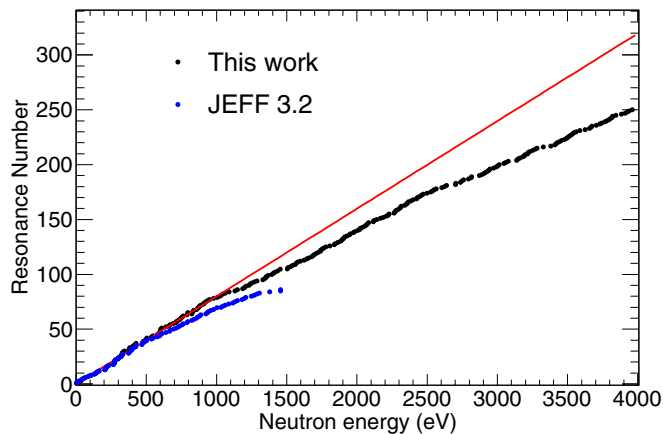
FIG. 14. Cumulative number of resonances as a function of the neutron energy showing a compatible D_0 for JEFF-3.2 and this work up to ~500 eV. The solid red line corresponds to the linear fit of this distribution in the energy region below 1.1 keV (see text for the details).

FIG. 15. Experimental distributions of reduced neutron widths together with a random simulated set of s- and p-wave resonances as a function of the neutron energy along with different thresholds for observation of resonances used in the study. The purple line corresponds to the threshold used to identify p-wave candidates (details in the text).

It shows an increasing fraction of resonances missed due to the reduced statistics with increasing energy. In this figure we see that JEFF-3.2 is in fairly good agreement with this work up to ~500 eV, while at higher energies new resonances are observed in this work. A linear fit to our data below 1.1 keV, shown in Fig. 14, indicates a value of $D_0 = 12.5(7)$ eV, but this estimate can be affected by missing s-wave resonances or p-wave resonances wrongly considered as s-wave.

The analysis of the number of observed p-wave and missing s-wave resonances as well as a realistic estimate of the level spacing from our data was carried out with the help of statistical model simulations. Several thousands of artificial resonance sequences were generated using the extracted values of S_0 and $\langle \Gamma_\gamma \rangle$ and the value of p-wave neutron strength function $S_1 = 2.07 \times 10^{-4}$ recommended by Rich *et al.* in Ref. [17] for a consistent description of the fast energy range with average neutron properties. These sequences were simulated for several different values of D_0 and the consistency of predictions with observables was checked assuming a threshold for observation in $g_J\Gamma_0$. The main goal of this study was to extract the expected number of s-wave resonances below the threshold and the number of p-wave resonances above the threshold from these simulations.

Actually, several different values of the threshold were tested. The lowest threshold T_{low} was estimated from the experimental data and corresponds to the weakest observed resonances. The medium and highest thresholds correspond to $T_{\text{med}} = 3 \times T_{\text{min}}$ and $T_{\text{hig}} = 5 \times T_{\text{min}}$, respectively. T_{low} and T_{hig} are shown in Fig. 15 together with the experimental distribution of reduced neutron widths and one random simulated sequence. In reality, $g_J\Gamma_0$ is shown on the vertical axis as the expectation value of this quantity is independent of the resonance spin (of p-wave resonances), and the SAMMY fit produces rather this quantity than Γ_0.

The predicted number of observable resonances for several different neutron energy ranges and three different values of the threshold are listed in Table VI for a few assumed values of D_0. The listed uncertainties in the predicted number of visible levels correspond to the standard deviation obtained from the analysis of the individual simulated resonance sequences. The ranges of D_0 values compatible with the experimental data within one standard deviation are presented at the bottom of the table.

A value of $D_0 = 15.8(8)$ eV, consistent with the observed number of levels for all the energy intervals and thresholds within ~1σ, is the proposed average spacing of s-wave resonances from our analysis. This value shows that the D_0 extracted directly from the number of observed levels below 1.1 keV (see the line in Fig. 14) is indeed biased by several observed p-wave resonances. The proposed value is significantly larger than the value in ENDF/B-VII.1 (13.6 eV) and RIPL [13.50(15) eV] and consistent with the value in JEFF-3.2 (15.3 eV) and the one proposed by Rich *et al.* [16.8(5) eV].

The consistency of experimental data—for cumulative number of observed resonances as a function of the neutron energy and the distribution of reduced neutron widths—with a few simulated sequences is shown in Fig. 16; the lowest threshold (labeled as T_{low} in Fig. 15) was used in this case.

According to our statistical analysis the total number of s-wave resonances below 4 keV is estimated to be 254(8). Assuming the lowest tested threshold, one can expect that about 46(4) s-wave resonances should be missing in our measurement while about 45(6) p-wave resonances should be observed. Focusing on the energy interval below 1.1 keV, where the simple plot (Fig. 14) indicates no missing levels, our simulations indicate that 21(4) p waves are to be observed and 5(2) s waves to be missed, leading to a too low predicted spacing.

Possible p-wave resonances, indicated in Table VIII, were identified according to statistical model simulations of the distribution of reduced neutron widths for the p-wave component. The distribution of $g_J\Gamma_0$ was calculated using $S_1 = 2.07 \times 10^{-4}$ [17], $D_1 = D_0/2$ from spin/parity arithmetics, and a

TABLE VI. Number of predicted and experimentally observed levels for three different maximum neutron energy ranges (600, 1000, and 3700 eV) and three different thresholds (T_{min} is the observation threshold, $T_{mid} = 3 \times T_{low}$ and $T_{hig} = 5 \times T_{low}$). The row labeled as "Range D_0" gives the interval of D_0 compatible within one standard deviation with the number of observed levels.

D_0 (eV)	T_{low}			T_{mid}			T_{high}		
	600 eV	1000 eV	4000 eV	600 eV	1000 eV	4000 eV	600 eV	1000 eV	4000 eV
12.5	54(5)	89(6)	290(12)	42(4)	69(5)	212(10)	41(4)	65(5)	184(10)
13.5	51(5)	86(6)	277(12)	40(4)	64(5)	200(10)	38(4)	61(5)	174(10)
14.5	49(5)	82(6)	266(11)	37(4)	60(5)	189(10)	35(4)	57(5)	166(9)
15.5	47(5)	79(6)	256(11)	35(4)	57(5)	180(9)	33(4)	54(5)	158(9)
16.5	45(5)	76(6)	247(11)	33(4)	54(5)	171(9)	31(3)	51(5)	150(9)
17.5	44(5)	73(6)	239(11)	32(3)	51(4)	164(9)	30(3)	48(4)	144(9)
18.5	42(5)	71(6)	233(11)	30(3)	49(4)	158(9)	28(3)	46(4)	139(8)
EXP.	48	78	251	32	56	187	31	54	155
RANGE D_0	12.9–17.5	13.9–18.1	14.9–17.3	15.3–18.9	14.5–17.3	13.9–16.1	14.9–18.7	14.1–16.7	14.7–17.1

channel radius $R = 1.35 \times A^{1/3} fm$ to compute the *p*-wave penetrability. The energy dependence of the average value of $g_J\Gamma_0$ was found to be $\langle g_J\Gamma_0 \rangle = 1.10 \times 10^{-8} E_n$, where E_n is

given in eV. According to the Porter-Thomas distribution there is only just 1% (0.35%) chance that one *p*-wave resonance has a $g_J\Gamma_0$ value larger than 6.64 (8.53) times the average.

The 0.35% *p*-wave limit, shown in Fig. 15, was used for labeling the resonance as possible *p* wave in Table VIII. This threshold was found to miss a negligible number of observable *p*-wave resonances while keeping small the number of *s*-wave resonances tagged as *p*-wave candidates. According to our analysis, the *p*-wave contribution is mainly observable below 2 keV, where we found 37 *p*-wave candidates out of a total of 43 in the full energy range. This result is consistent with the 31(5) and 9(3) candidate resonances with *p*-wave and *s*-wave origin, respectively, predicted by the simulations below 2 keV. Among the *p*-wave candidates we find the ten observed resonances below 500 eV considered as *p*-wave in ENDF/B-VII.1 (considered *s*-wave in JEFF-3.2).

The average resonance parameters extracted from the analysis of the resonance region of the radiative capture cross section of ^{242}Pu are compared to previous values in the literature in Fig. 17 and listed in Table VII. The larger energy range and number of resonances analyzed in this work reduces the

FIG. 16. Top: Experimental cumulative energy distribution of observed resonances compared to several sequences obtained from statistical model simulations showing the good reproduction of the data. Bottom: Experimental cumulative distribution of reduced neutron widths of all observed levels compared to several simulated sequences showing again a very good agreement. The simulations were performed with $D_0 = 15.8$ eV, $S_0 = 0.91 \times 10^{-4}$, and $S_1 = 2.07 \times 10^{-4}$ [17] and the minimum threshold was used.

FIG. 17. Average resonance parameters obtained in this work (n_TOF) compared to the values in the literature: S_0 (left), D_0 (middle), $\langle\Gamma_\gamma\rangle$ (right). The shadowed area corresponds to the uncertainty from our analysis.

TABLE VII. Average resonance parameters of the ^{242}Pu(n,γ) cross section obtained in this work compared to the values in the literature.

	$10^4 \times S_0$	D_0 (eV)	$\langle \Gamma_\gamma \rangle$ (meV)
ENDF/B-VII.1 [9]	1.02	13.6	22.27
JEFF-3.2 [10]	1.00	15.3	24.2
JENDL-4.0 [15]	0.98	–	23.4
RIPL [16]	0.98(8)	13.50(15)	23.0(20)
Rich *et al.* [17]	0.91(20)	16.8(5)	22.0(10)
This work	0.91(8)	15.8(8)	24.8(5)

uncertainty of these parameters with respect to previous measurements and should help to solve previous discrepancies.

VI. SUMMARY AND OUTLOOK

The neutron capture cross section of ^{242}Pu has been measured by means of the time-of-flight technique at the CERN n_TOF-EAR1 facility employing an array of four C_6D_6 scintillators as a detection system. The target consisted of seven thin layers of ^{242}Pu enriched to 99.959%, each of 45 mm in diameter, with a total mass of 95(4) mg electrodeposited on thin aluminum backings. The capture data cover the neutron energy interval from thermal to few hundreds of keV.

This paper deals with the analysis of the data below a neutron energy of 4 keV. A detailed description of the analysis and quality assurance methods leading to a capture cross section with a systematic uncertainty of 5% is given. This uncertainty meets th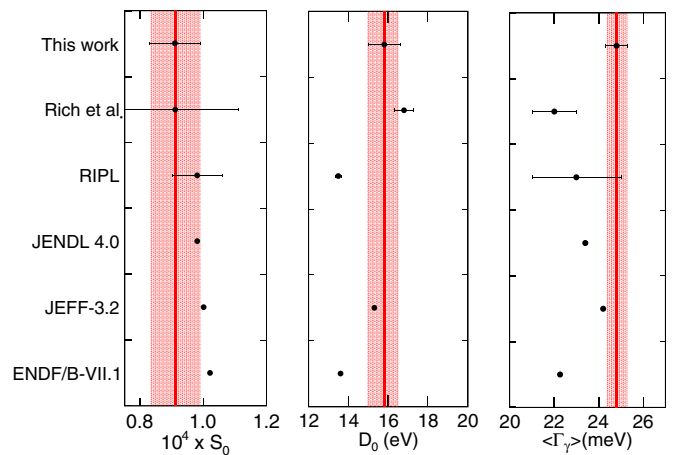e requirements of the NEA-HPRL. The good energy resolution of the facility and the accumulated statistics have allowed us to observe individual resonances and determine their parameters up to 4 keV, while resonance parameters from capture measurements were previously reported only below 1.3 keV. The individual resonance parameters of 251 resonance have been extracted, 180 of which had never been reported before in any neutron radiative capture measurement. The data presented in this work indicate a ∼4% higher capture cross section compared to JEFF-3.2 in terms of weighted average of resonance kernels ratio (∼6% higher compared to

the new measurement at DANCE). In particular, for the 2.67 eV resonance the obtained radiative kernel is 4.2% larger than in the evaluations, while DANCE reports a resonance integral 2.4% larger than ENDF/B-VII.1.

The large set of analyzed resonances has led to a value of S_0 more accurate than those of previous experiment and compatible with the values in the literature. A higher value of $\langle \Gamma_\gamma \rangle$, compatible just with JEFF-3.2 and RIPL was extracted from our analysis. Statistical simulations indicate that the low threshold for observation allows the strongest p-wave resonances to be observed, especially below 2 keV, while some of s-wave resonances remain unobservable. The analysis of the observed number of resonances using such simulations leads to a value of D_0 consistent with JEFF-3.2 and with the value proposed by Rich *et al.* but significantly larger than the value in ENDF/B-VII.1 and RIPL.

In summary, the new high-resolution capture data allow us to meet the requirements of the NEA-HPRL in terms of reduction of the current uncertainty in the capture cross section of ^{242}Pu and shall lead to a revised evaluation with an improved accuracy of 5% in the resolved resonance region up to 4 keV and a larger set of resonance parameters.

The obtained capture yield extends up to at least 200 keV, covering a large fraction of the unresolved resonance region. The analysis of this higher-energy region is ongoing and is a subject for future research.

APPENDIX: LIST OF INDIVIDUAL RESONANCE PARAMETERS AND RADIATIVE KERNELS

TABLE VIII. Individual resonance parameters and radiative kernels of the ^{242}Pu(n,γ) cross section obtained in this work. The uncertainties listed in the table are only statistical and have been obtained from the SAMMY calculations.

Energy (eV)	J	Γ_γ (meV)	$g_J \Gamma_n$ (meV)	Γ_f (meV)	R_K (meV)	n_TOF/JEFF	n_TOF/DANCE
2.67625(3)[a]	0.5	25.4(6)	2.0965(19)	0.002	1.936(4)	1.0428(21)	1.036(19)
22.569(10)[a]	0.5	24.8	0.297(3)	0.01	0.293(3)	1.041(10)	1.14(4)
32.952(17)[b,d]	(0.5)	24.8	0.0199(22)	0.01	0.0199(22)	–	–
40.951(20)[a]	0.5	24.8	0.47(6)	0.01	0.461(6)	1.038(14)	1.12(4)
53.4649(8)[a]	0.5	24.1(3)	56.1(14)	0.0019	16.86(20)	1.029(12)	1.07(3)
67.628(12)[a]	0.5	24.8	4.68(4)	0.0445	3.95(3)	1.04(8)	1.11(3)
88.469(6)[a]	0.5	24.8	0.591(19)	0.0382	0.577(18)	0.93(3)	0.81(7)
107.3824(15)[a]	0.5	24.8	17.48(20)	0.0494	10.36(7)	1.093(7)	0.95(6)
131.446(3)[a]	0.5	24.8	6.39(9)	0.0635	5.1(6)	0.994(11)	0.87(7)
141.34(5)[a,d,e]	(0.5)	24.8	0.124(21)	0.01	0.123(21)	1.04(17)	1.04(21)

TABLE VIII. (*Continued.*)

Energy (eV)	J	Γ_γ (meV)	$g_J \Gamma_n$ (meV)	Γ_f (meV)	R_K (meV)	n_TOF/JEFF	n_TOF/DANCE
149.838(3)[a]	0.5	24.8	13.71(20)	0.0554	8.9(8)	0.983(9)	1.19(10)
163.69(21)[a]	0.5	24.8	0.49(4)	0.01	0.48(4)	0.91(7)	0.93(11)
205.022(3)[a]	0.5	23.7(3)	52.0(19)	0.0548	16.29(24)	1.093(16)	1.10(6)
210.24(5)[a]	0.5	24.8	0.3(4)	0.01	0.29(4)	0.7(10)	0.71(12)
215.488(7)[a]	0.5	24.8	5.48(14)	0.184	4.48(9)	0.991(21)	0.89(7)
219.54(6)[a,d,e]	(0.5)	24.8	0.28(4)	0.01	0.28(4)	0.97(15)	1.10(9)
232.942(8)[a]	0.5	24.8	5.61(17)	0.131	4.58(11)	1.09(3)	1.19(21)
264.7(7)[a,d,e]	(0.5)	24.8	0.36(6)	0.01	0.36(6)	0.95(16)	1.00(19)
272.41(8)[a,d,e]	(0.5)	24.8	0.32(6)	0.01	0.32(6)	1.9(4)	2.0(4)
273.786(7)[a]	0.5	24.8	14.8(5)	0.102	9.35(19)	1.001(20)	0.97(7)
275.07(9)[a,d,e]	(0.5)	24.8	0.27(6)	0.01	0.27(6)	1.6(4)	1.6(4)
281.2(13)[a,d,e]	(0.5)	24.8	0.16(5)	0.01	0.16(5)	1.3(4)	1.2(4)
298.873(10)[a]	0.5	24.8	9(3)	0.01	6.65(18)	1.06(3)	1.04(9)
303.727(8)[a]	0.5	26.6(13)	17.8(5)	0.067	10.6(3)	1.09(3)	1.04(7)
317.53(11)[b,d]	(0.5)	24.8	0.33(9)	0.01	0.33(8)	–	–
320.096(7)[a]	0.5	26.7(4)	230(16)	0.017	23.9(4)	1.121(17)	1.36(5)
328.97(14)[b,d]	(0.5)	24.8	0.2(8)	0.01	0.2(8)	–	–
332.642(8)[a]	0.5	28.5(7)	70(5)	0.018	20.3(6)	0.95(3)	0.97(8)
341.97(13)[b,d]	(0.5)	24.8	0.39(1)	0.01	0.39(11)	–	–
374.484(19)[a]	0.5	24.8	6.2(3)	0.01	5(19)	0.99(4)	0.96(9)
380.52(19)[a,d,e]	(0.5)	24.8	0.18(7)	0.01	0.18(7)	0.7(3)	0.7(3)
382.548(10)[a]	0.5	22.7(6)	50(4)	0.085	15.6(5)	1.02(3)	0.98(7)
400.19(4)[a]	0.5	24.8	1.97(18)	0.01	1.83(16)	1.21(10)	1.10(14)
410.845(18)[a]	0.5	24.8	8.7(4)	0.01	6.47(23)	1.15(4)	1.05(9)
424.27(3)[a]	0.5	24.8	4.6(3)	0.18	3.86(19)	1.11(5)	1.11(11)
425.68(17)[a,d,e]	(0.5)	24.8	0.31(11)	0.01	0.31(11)	1.1(4)	1.1(4)
468.42[f,c,d]	0.5	24.2	0.03	30	–	–	–
473.73(9)[a,e]	0.5	24.8	1.2(19)	0.32	1.13(17)	1.24(19)	1.20(22)
482.896(16)[a]	0.5	28.2(17)	23.5(12)	0.42	12.7(5)	1.16(5)	1.13(9)
486.97(19)[b,d]	(0.5)	24.8	0.34(12)	0.01	0.34(12)	–	–
495.11(21)[a,d,e]	(0.5)	24.8	0.29(12)	0.01	0.29(11)	1.1(4)	1.08(4)
504.033(21)[g]	0.5	24.8	29(6)	0.19	13.6(13)	–	–
504.749(16)[g,b]	0.5	24.8	60(10)	0.19	17.9(9)	–	–
536.81(14)[a]	0.5	25.9(8)	96(11)	0.043	20.4(7)	1.18(4)	–
548.81(17)[a]	0.5	22.3(9)	74(10)	0.077	17.1(8)	0.92(4)	–
576.532(16)[a]	0.5	24.8	44(4)	0.01	16.2(5)	1.21(4)	–
591.02(15)[b,d]	(0.5)	24.8	1.02(24)	0.01	0.98(22)	–	–
595.427(20)[a]	0.5	28.2(17)	38(3)	0.021	16.2(8)	1.28(6)	–
598.65(18)[b,d]	(0.5)	24.8	0.95(25)	0.021	0.92(23)	–	–
600.21(3)[a]	0.5	24.8	10.4(8)	0.102	7.3(4)	1.11(6)	–
604.48(16)[b,d]	(0.5)	24.8	0.99(24)	0.1	0.95(22)	–	–
611.14(3)[a]	0.5	24.8	13.1(10)	0.064	8.6(4)	1.08(6)	–
639.44(7)[a]	0.5	24.8	4.3(4)	0.04	3.7(3)	0.98(9)	–
660.27(13)[b,d]	(0.5)	24.8	0.78(22)	0.066	0.76(20)	–	–
670.28(3)[a]	0.5	24.8	15.5(13)	0.051	9.6(5)	1.14(6)	–
693.56(3)[a]	0.5	29.1(20)	40(4)	0.24	16.8(9)	1.25(7)	–
712.18(3)[a]	0.5	25.9(11)	121(29)	0.163	21.3(12)	1.27(7)	–
713.9(16)[b,d]	(0.5)	24.8	1.6(4)	0.01	1.5(3)	–	–
727.71(9)[a]	0.5	24.8	3.8(5)	0.05	3.3(4)	1.17(14)	–
737.23(3)[a]	0.5	26.1(12)	105(20)	0.45	20.8(11)	1.06(6)	–
748.04(19)[b,d]	(0.5)	24.8	1.3(3)	0.05	1.2(3)	–	–
755.75(3)[a,c]	0.5	21.5	130	1.6	–	–	–
762.8(5)[a,c]	0.5	24.2	5.6	440	–	–	–
789.28(4)[a,c]	0.5	24.2	64	1.6	–	–	–
794.52(3)[a]	0.5	24.7(11)	201(78)	0.043	22(13)	1.02(6)	–
825.28(9)[a]	0.5	24.8	6(8)	0.21	4.8(5)	1.24(14)	–
831.91(21)[b,d]	(0.5)	24.8	1.4(4)	0.01	1.3(4)	–	–

TABLE VIII. (*Continued.*)

Energy (eV)	J	Γ_γ (meV)	$g_J\Gamma_n$ (meV)	Γ_f (meV)	R_K (meV)	n_TOF/JEFF	n_TOF/DANCE
838.45(4)[a]	0.5	25.3(21)	39(5)	0.041	15.3(11)	1.17(8)	–
857.09(4)[a]	0.5	27(3)	34(4)	0.093	15.2(11)	1.13(8)	–
866.38(6)[a]	0.5	24.8	12.5(14)	0.043	8.4(6)	1.16(9)	–
873.74(11)[b]	0.5	24.8	6.1(9)	0.043	4.9(6)	–	–
879.64(4)[a]	0.5	23.2(17)	59(10)	0.027	16.6(12)	0.97(7)	–
887.31(5)[a]	0.5	28(4)	23.0(24)	0.0155	12.6(11)	0.99(8)	–
908.4(3)[b,d]	(0.5)	24.8	0.8(3)	0.01	0.8(3)	–	–
913.31(21)[b,d]	(0.5)	24.8	1.8(5)	0.01	1.7(4)	–	–
923.73(5)[a]	0.5	21.4(17)	59(12)	0.029	15.7(12)	1.14(9)	–
936.76(8)[a]	0.5	24.8	10.8(15)	0.01	7.6(7)	1(9)	–
950.35(8)[a]	0.5	24.8	12.4(16)	0.01	8.4(7)	0.92(8)	–
978.81(8)[a]	0.5	24.8	12.9(18)	0.01	8.6(8)	0.94(9)	–
1005.34(5)[a]	0.5	31(3)	43(6)	0.01	18.0(15)	1.16(9)	–
1024.04(25)[b,d]	(0.5)	24.8	2.2(7)	0.01	2(6)	–	–
1031.36(5)[a]	0.5	23.4(23)	46(8)	0.01	15.5(14)	0.98(9)	–
1046.19(6)[a]	0.5	20.6(15)	118(47)	0.01	17.5(15)	0.87(8)	–
1063.55(6)[a]	0.5	24.8	44(8)	0.01	16.2(10)	1.16(7)	–
1088.99(6)[a]	0.5	27.4(16)	200(77)	0.01	24.1(17)	1.12(8)	–
1130.47(12)[a]	0.5	24.8	12.7(20)	0.01	8.5(9)	1.2(13)	–
1148.96(7)[a]	0.5	23.4(14)	300(146)	0.01	21.7(14)	0.97(6)	–
1185.47(13)[a]	0.5	24.8	11.4(19)	0.01	7.9(9)	0.93(11)	–
1198.78(7)[a]	0.5	23.2(20)	95(33)	0.01	18.6(18)	0.97(9)	–
1207.75(7)[a]	0.5	24.8	49(10)	0.01	16.7(12)	1.11(8)	–
1229.92(15)[b]	0.5	24.8	8.8(18)	0.01	6.6(10)	–	–
1239.1(3)[b,d]	(0.5)	24.8	2.3(8)	0.01	2.1(7)	–	–
1249.31(14)[a]	0.5	24.8	11.1(20)	0.01	7.8(10)	1.18(15)	–
1268.96(10)[a]	0.5	24.8	26(5)	0.01	12.9(11)	1.01(9)	–
1288.33(9)[a]	0.5	23(3)	59(16)	0.01	16.6(18)	0.97(10)	–
1330.64(9)[b]	0.5	24.8	67(20)	0.01	18.5(15)	–	–
1342.22(10)[b]	0.5	24.8	33(7)	0.01	14.3(13)	–	–
1351.5(4)[b,d]	(0.5)	24.8	1.7(8)	0.01	1.6(7)	–	–
1354.03(14)[b]	0.5	24.8	18(4)	0.01	10.5(13)	–	–
1368.19(8)[b]	0.5	24.8	210(95)	0.01	22.7(11)	–	–
1393.75(25)[b]	0.5	24.8	6.2(16)	0.01	5.0(10)	–	–
1405.81(25)[b]	0.5	24.8	6.5(16)	0.01	5.2(10)	–	–
1414.3(4)[b,d]	(0.5)	24.8	2.1(8)	0.01	2(7)	–	–
1433.3(14)[b]	0.5	24.8	19(4)	0.01	10.9(14)	–	–
1455.55(9)[b]	0.5	24.8	103(40)	0.01	20.4(16)	–	–
1503.71(17)[b]	0.5	24.8	17(4)	0.01	10.3(14)	–	–
1509.97(19)[b]	0.5	24.8	12(3)	0.01	8.2(13)	–	–
1527.4(3)[b,d]	(0.5)	24.8	3.9(14)	0.01	3.4(10)	–	–
1540.04(21)[b]	0.5	24.8	12(3)	0.01	8(13)	–	–
1560.5(3)[b,d]	(0.5)	24.8	4.6(16)	0.01	3.9(12)	–	–
1567.35(12)[b]	0.5	24.8	499(195)	0.01	24.3(5)	–	–
1578.5(3)[b,d]	(0.5)	24.8	5.1(15)	0.01	4.3(11)	–	–
1598.4(4)[b]	0.5	24.8	7.2(22)	0.01	5.6(13)	–	–
1623.39(12)[b]	0.5	24.8	106(42)	0.01	20.5(16)	–	–
1642.26(13)[b]	0.5	24.8	62(21)	0.01	18.1(17)	–	–
1654.26(22)[b]	0.5	24.8	15(4)	0.01	9.6(15)	–	–
1675.8(3)[b]	0.5	24.8	7.1(20)	0.01	5.6(12)	–	–
1687.7(3)[b]	0.5	24.8	8.4(24)	0.01	6.3(13)	–	–
1696.7(14)[b]	0.5	24.8	55(18)	0.067	17.4(18)	–	–
1708.93(13)[b]	0.5	24.8	199(85)	0.001	22.6(11)	–	–
1723.9(4)[b,d]	(0.5)	24.8	3.7(14)	0.1	3.2(11)	–	–
1739.9(4)[b,d]	(0.5)	24.8	7(3)	0.1	5.3(17)	–	–
1740.7(3)[b]	0.5	24.8	9(3)	0.1	6.4(18)	–	–
1752.6(3)[b]	0.5	24.8	8.6(25)	0.51	6.3(13)	–	–

TABLE VIII. (*Continued.*)

Energy (eV)	J	Γ_γ (meV)	$g_J \Gamma_n$ (meV)	Γ_f (meV)	R_K (meV)	n_TOF/JEFF	n_TOF/DANCE
1763.6(18)[b]	0.5	24.8	37(10)	0.017	15.1(17)	–	–
1779(4)[b,d]	(0.5)	24.8	6.3(21)	0.51	4.9(13)	–	–
1807.4(3)[b]	0.5	24.8	7.6(23)	0.13	5.9(13)	–	–
1838.1(4)[c]	0.5	–	–	–	–	–	–
1845.8(3)[b]	0.5	24.8	11(3)	0.01	7.6(15)	–	–
1863.11(20)[b]	0.5	24.8	34(10)	0.49	14.4(17)	–	–
1882.81(17)[b]	0.5	24.8	303(130)	0.056	23.5(8)	–	–
1892.2(3)[b]	0.5	24.8	15(4)	0.96	9.4(16)	–	–
1897.3(4)[b,d]	(0.5)	24.8	7(3)	1	5.6(15)	–	–
1906.05(22)[b]	0.5	24.8	33(11)	0.01	14.4(20)	–	–
1914(4)[b,d]	(0.5)	24.8	5.6(21)	0.01	4.6(14)	–	–
1928.82(18)[b]	0.5	24.8	361(159)	0.01	23.8(7)	–	–
1947.2(4)[b,d]	(0.5)	24.8	6.3(24)	0.01	5.1(15)	–	–
1953.2(4)[b,d]	(0.5)	24.8	5.5(21)	0.01	4.5(14)	–	–
1974.6(3)[b]	0.5	24.8	10(3)	0.01	7.2(18)	–	–
1983.85(19)[b]	0.5	24.8	71(27)	0.01	18.8(19)	–	–
2006.25(20)[b]	0.5	24.8	86(35)	0.01	19.6(18)	–	–
2018.2(4)[b,d]	(0.5)	24.8	9(3)	0.01	6.6(18)	–	–
2023.35(19)[b]	0.5	24.8	187(88)	0.01	22.4(13)	–	–
2038.41(20)[b]	0.5	24.8	99(41)	0.01	20.3(17)	–	–
2057.21(19)[b]	0.5	24.8	183(86)	0.01	22.4(13)	–	–
2068.1(4)[b]	0.5	24.8	9(3)	0.01	6.7(19)	–	–
2074.5(4)[b]	0.5	24.8	12(4)	0.01	8(19)	–	–
2082.2(4)[b]	0.5	24.8	13(4)	0.01	8.5(20)	–	–
2115.71(23)[b]	0.5	24.8	77(31)	0.01	19.1(20)	–	–
2121(3)[b]	0.5	24.8	18(6)	0.01	10.4(21)	–	–
2141.1(4)[b]	0.5	24.8	11(4)	0.01	7.6(20)	–	–
2166.5(3)[b]	0.5	24.8	21(7)	0.01	11.6(22)	–	–
2186.8(23)[b]	0.5	24.8	120(53)	0.01	21(16)	–	–
2209.9(3)[b]	0.5	24.8	47(18)	0.01	16.6(22)	–	–
2223.3(3)[b]	0.5	24.8	28(10)	0.01	13.2(23)	–	–
2229.6(4)[b]	0.5	24.8	12(5)	0.01	8(22)	–	–
2265.2(3)[b]	0.5	24.8	37(14)	0.01	15.1(23)	–	–
2271(4)[b]	0.5	24.8	13(5)	0.01	8.4(22)	–	–
2276.5(3)[b]	0.5	24.8	226(108)	0.01	22.9(11)	–	–
2291.8(5)[b,d]	(0.5)	24.8	8(3)	0.01	6.3(19)	–	–
2303.7(3)[b]	0.5	24.8	36(14)	0.01	14.8(24)	–	–
2311.3(3)[b]	0.5	24.8	239(119)	0.01	23(11)	–	–
2315(4)[b]	0.5	24.8	18(7)	0.01	10.4(25)	–	–
2338.6(3)[b]	0.5	24.8	86(39)	0.01	19.7(21)	–	–
2351.9(5)[b]	0.5	24.8	43(22)	0.01	16(3)	–	–
2359.9(4)[b]	0.5	24.8	14(6)	0.01	9.1(23)	–	–
2366.9(5)[b]	0.5	24.8	12(5)	0.01	8.1(22)	–	–
2384.6(4)[b]	0.5	24.8	19(7)	0.01	11(24)	–	–
2401.6(4)[b]	0.5	24.8	33(13)	0.01	14.4(25)	–	–
2424.7(4)[b]	0.5	24.8	14(6)	0.01	9.2(25)	–	–
2431.1(4)[b]	0.5	24.8	17(7)	0.01	10.1(24)	–	–
2446.4(4)[b]	0.5	24.8	34(14)	0.01	14.7(25)	–	–
2459.7(4)[b]	0.5	24.8	21(8)	0.01	11.6(25)	–	–
2471(4)[b]	0.5	24.8	41(17)	0.01	15.8(24)	–	–
2497.9(3)[b]	0.5	24.8	88(39)	0.01	19.8(20)	–	–
2525.7(5)[b]	0.5	24.8	12(5)	0.01	8.3(23)	–	–
2538.9(4)[b]	0.5	24.8	18(7)	0.01	11(3)	–	–
2549.4(5)[b]	0.5	24.8	19(7)	0.01	10.7(24)	–	–
2563.7(3)[b]	0.5	24.8	178(83)	0.01	22.3(13)	–	–
2605.2(4)[b]	0.5	24.8	39(16)	0.01	15.5(24)	–	–

TABLE VIII. (*Continued.*)

Energy (eV)	J	Γ_γ (meV)	$g_J\Gamma_n$ (meV)	Γ_f (meV)	R_K (meV)	n_TOF/JEFF	n_TOF/DANCE
2623(4)[b]	0.5	24.8	17(8)	0.01	10(3)	–	–
2637.4(3)[b]	0.5	24.8	230(108)	0.01	23(11)	–	–
2702.6(5)[b]	0.5	24.8	167(82)	0.11	22.1(14)	–	–
2703.6(5)[b]	0.5	24.8	147(71)	0.11	21.7(15)	–	–
2736.2(4)[b]	0.5	24.8	163(73)	0.094	22(13)	–	–
2745.5(6)[b,d]	(0.5)	24.8	11(4)	1.5	7.3(19)	–	–
2758.7(4)[b]	0.5	24.8	124(61)	0.031	21.1(18)	–	–
2794.2(5)[b]	0.5	24.8	28(11)	0.01	13(3)	–	–
2811.1(5)[b]	0.5	24.8	14(7)	0.01	9(3)	–	–
2816.8(5)[b]	0.5	24.8	23(10)	0.01	12(3)	–	–
2871.6(4)[b]	0.5	24.8	494(237)	0.01	24.2(6)	–	–
2889.5(5)[b]	0.5	24.8	19(9)	0.01	11(3)	–	–
2904.8(5)[b]	0.5	24.8	21(10)	0.01	12(3)	–	–
2916.5(4)[b]	0.5	24.8	249(118)	0.01	23.1(10)	–	–
2931.7(5)[b]	0.5	24.8	44(19)	0.01	16(3)	–	–
2941.3(4)[b]	0.5	24.8	63(28)	0.01	18.1(23)	–	–
2947.7(4)[b]	0.5	24.8	68(31)	0.01	18.6(23)	–	–
2974.3(4)[b]	0.5	24.8	86(39)	0.01	19.7(20)	–	–
2993.9(4)[b]	0.5	24.8	68(30)	0.01	18.5(22)	–	–
3002.7(4)[b]	0.5	24.8	115(57)	0.01	20.9(19)	–	–
3012.6(5)[b]	0.5	24.8	34(15)	0.01	15(3)	–	–
3045.6(5)[b]	0.5	24.8	21(10)	0.01	11(3)	–	–
3058.4(5)[b]	0.5	24.8	60(28)	0.01	18(3)	–	–
3076.8(5)[b]	0.5	24.8	89(41)	0.01	19.8(20)	–	–
3137.3(5)[b]	0.5	24.8	62(28)	1.2	17.8(24)	–	–
3145(5)[b]	0.5	24.8	340(167)	1.22	23.6(8)	–	–
3159.1(5)[b]	0.5	24.8	143(67)	0.01	21.6(15)	–	–
3178.6(5)[b]	0.5	24.8	85(39)	0.01	19.6(21)	–	–
3192.5(6)[b,d]	(0.5)	24.8	16(7)	0.01	10(3)	–	–
3197(5)[b]	0.5	24.8	37(17)	0.01	15(3)	–	–
3215.8(6)[b]	0.5	24.8	40(19)	0.01	16(3)	–	–
3219.5(5)[b]	0.5	24.8	112(55)	0.01	20.8(19)	–	–
3228.5(5)[b]	0.5	24.8	62(29)	0.01	18.1(24)	–	–
3250.6(5)[b]	0.5	24.8	68(31)	0.01	18.5(23)	–	–
3270.1(5)[b]	0.5	24.8	52(24)	0.01	17(3)	–	–
3282.5(5)[b]	0.5	24.8	55(26)	0.01	17(3)	–	–
3326.3(5)[b]	0.5	24.8	188(90)	0.01	22.5(13)	–	–
3378.8(5)[b]	0.5	24.8	72(34)	0.01	18.8(23)	–	–
3408.7(6)[b]	0.5	24.8	25(12)	0.01	13(3)	–	–
3416.9(5)[b]	0.5	24.8	187(97)	0.009	22.4(14)	–	–
3426.3(6)[b]	0.5	24.8	51(24)	0.01	17(3)	–	–
3442.4(6)[b]	0.5	24.8	31(14)	0.01	14(3)	–	–
3456.7(5)[b]	0.5	24.8	233(116)	0.13	23(11)	–	–
3477.7(5)[b]	0.5	24.8	118(57)	0.11	21(18)	–	–
3491.7(6)[b]	0.5	24.8	105(52)	0.28	20.5(20)	–	–
3501.4(6)[b]	0.5	24.8	236(115)	0.36	23(11)	–	–
3513.1(5)[b]	0.5	24.8	127(60)	0.01	21.2(17)	–	–
3524.8(5)[b]	0.5	24.8	157(76)	0.2	21.9(15)	–	–
3533.6(6)[b]	0.5	24.8	59(28)	0.01	18(3)	–	–
3545.5(6)[b]	0.5	24.8	28(14)	0.01	13(3)	–	–
3560.8(6)[b]	0.5	24.8	43(20)	0.01	16(3)	–	–
3586.8(6)[b]	0.5	24.8	321(156)	0.18	23.6(8)	–	–
3624.9(7)[b,d]	(0.5)	24.8	12(6)	0.29	8(3)	–	–
3656.1(6)[b]	0.5	24.8	161(79)	0.67	21.9(15)	–	–
3664.8(6)[b]	0.5	24.8	40(20)	0.01	16(3)	–	–
3674.2(6)[c]	0.5	–	–	–	–	–	–
3705.3(7)[b,d]	(0.5)	24.8	14(7)	0.01	9(3)	–	–

TABLE VIII. (*Continued.*)

Energy (eV)	J	Γ_γ (meV)	$g_J\Gamma_n$ (meV)	Γ_f (meV)	R_K (meV)	n_TOF/JEFF	n_TOF/DANCE
3727.9(6)[b]	0.5	24.8	200(180)	0.05	22.7(15)	–	–
3742.3(6)[b]	0.5	24.8	76(36)	0.01	19.1(23)	–	–
3764.1(6)[b]	0.5	24.8	48(23)	0.01	17(3)	–	–
3777.4(7)[b]	0.5	24.8	370(182)	0.21	23.8(8)	–	–
3794.7(6)[b]	0.5	24.8	84(40)	0.07	19.5(22)	–	–
3806.3(6)[b]	0.5	24.8	70(34)	0.07	18.7(24)	–	–
3816.5(7)[b]	0.5	24.8	115(55)	0.015	20.9(18)	–	–
3818.6(6)[b]	0.5	24.8	452(229)	0.015	24.1(7)	–	–
3841.3(7)[b,g]	0.5	24.8	37(25)	0.05	15(4)	–	–
3843.7(6)[b,g]	0.5	24.8	57(35)	0.05	18(3)	–	–
3882.5(6)[b]	0.5	24.8	88(42)	0.01	19.8(21)	–	–
3909.3(7)[b]	0.5	24.8	25(12)	0.01	13(3)	–	–
3926.2(6)[b]	0.5	24.8	64(31)	0.01	18.3(25)	–	–
3938.3(6)[b]	0.5	24.8	57(27)	0.01	18(3)	–	–
3959.6(6)[b]	0.5	24.8	72(37)	0.01	19(3)	–	–

[a]Included in JEFF-3.2.

[b]Not included in JEFF-3.2.

[c]Large (Non-negligible) fission width: Not analyzed, parameters in the table from JEFF-3.2 ($E_n < 1.3$ keV).

[d]*p*-wave candidate: Spin could not be assigned.

[e]*p*-wave resonance in ENDF/B-VII.1.

[f]Resonance in JEFF-3.2 below the experimental threshold in Γ_0: Neither confirmed nor rejected.

[g]Doublet. Just one resonance in JEFF-3.2 or in previous measurements.

[1] Status and Advances in MOX Fuel Technology, IAEA Technical Reports Series No. 415 (2003).

[2] N. Colonna *et al.*, Energy Environ. Sci. **3**, 1910 (2010).

[3] M. Salvatores and R. Jacqmin, Uncertainty and target accuracy assessment for innovative system using recent covariance data evaluations, Tech. Rep., NEA/WPEC-26, Argonne National Laboratory (2008).

[4] F. Poortmans *et al.*, Nucl. Phys. A **207**, 342 (1973).

[5] R. W. Hockenbury *et al.*, Natl. Bur. Stands. (U.S.), Spec. Publ. **425**, 584 (1975).

[6] K. Wisshak and F. Kaeppeler, Nucl. Sci. Eng. **66**, 363 (1978).

[7] K. Wisshak and F. Kaeppeler, Nucl. Sci. Eng. **69**, 39 (1979).

[8] M. Q. Buckner, C. Y. Wu, R. A. Henderson, B. Bucher, A. Chyzh, T. A. Bredeweg, B. Baramsai, A. Couture, M. Jandel, S. Mosby, J. M. ODonnell, and J. L. Ullmann, Phys. Rev. C **93**, 044613 (2016).

[9] M. B. Chadwick *et al.*, Nucl. Data Sheets **112**, 2887 (2011).

[10] A. Santamarina, D. Bernard, P. Blaise, M. Coste, A. Courcelle, T. D. Huynh, C. Jouanne, P. Leconte, O. Litaize, S. Mengelle, G. Noguère, J.-M. Ruggiéri, O. Sérot, J. Tommasi, C. Vaglio, and J.-F. Vidal, The JEFF3.1.1 nuclear data library, JEFF Report No. 22, OECD/Nuclear Energy Agency (2009).

[11] G. Noguere, E. Dupont, J. Tommasi, and D. Bernard, Nuclear data needs for actinides by comparison withpost irradiation experiments, Technical note CEA Cadarache, NT-SPRC/LEPH-05/204 (2005).

[12] J. Tommasi, E. Dupont, and P. Marimbeau, Nucl. Sci. Eng. **154**, 119 (2006).

[13] J. Tommasi and G. Noguere, Nucl. Sci. Eng. **160**, 232 (2008).

[14] NEA Nuclear Data High Priority Request List, www.oecd-nea.org/dbdata/hprl/

[15] K. Shibata *et al.*, J. Nucl. Sci. Technol. **48**, 1 (2011).

[16] R. Capote *et al.*, Nucl. Data Sheets **110**, 3107 (2009).

[17] E. Rich *et al.*, Nucl. Sci. Eng. **162**, 178 (2009).

[18] C. Guerrero, E. Mendoza *et al.*, CERN-INTC-2013-027/INTC-P-387 (2013).

[19] J. Lerendegui-Marco *et al.*, EPJ Web Conf. **111**, 02005 (2016).

[20] J. Lerendegui-Marco *et al.*, EPJ Web Conf. **146**, 11045 (2017).

[21] C. Guerrero *et al.*, Eur. Phys. J. A **49**, 27 (2013).

[22] C. Weiss *et al.*, Nucl. Instrum. Meth. A **799**, 90 (2015).

[23] J. Lerendegui-Marco, S. Lo Meo, C. Guerrero *et al.*, Eur. Phys. J. A **52**, 100 (2016).

[24] M. Barbagallo *et al.* (The n_TOF Collaboration), Phys. Rev. Lett. **117**, 152701 (2016).

[25] CHANDA: solving CHAllenges in Nuclear DAta. Project funded by FP7-EURATOM-FISSION, EC (Grant No. 605203).

[26] K. Eberhardt *et al.*, Chemical purification of plutonium and preparation of ^{242}Pu-targets by Molecular Plating, CHANDA-Workshop, PSI (Villigen, Switzerland), November 23–25, 2015.

[27] C. Guerrero *et al.*, Phys. Rev. C **85**, 044616 (2012).

[28] E. Mendoza *et al.*, Phys. Rev. C **90**, 034608 (2014).

[29] E. Mendoza *et al.*, Nucl. Data Sheets **119**, 65 (2014).

[30] R. Macklin, J. Halperin, and R. Winters, Nucl. Instrum. Meth. A **164**, 213 (1979).

[31] C. Guerrero *et al.*, Nucl. Instrum. Meth. A **608**, 424 (2009).

[32] R. Plag *et al.*, Nucl. Instrum. Meth. A **496**, 425 (2003).

[33] J. Allison *et al.*, IEEE Trans. Nucl. Sci. **53**, 270 (2006).

[34] J. Allison *et al.*, Nucl. Instrum. Meth. A **835**, 186 (2016).

[35] S. Marrone *et al.*, Nucl. Instrum. Meth. A **517**, 389 (2004).

[36] U. Abondanno *et al.*, Nucl. Instrum. Meth. A **538**, 692 (2004).

[37] P. Žugec *et al.*, Nucl. Instrum. Meth. A **812**, 134 (2016).

[38] C. Guerrero *et al.*, Nucl. Instrum. Meth. A **597**, 212 (2008).

[39] G. Lorusso *et al.*, Nucl. Instrum. Meth. A **532**, 622 (2004).

[40] R. L. Macklin and J. H. Gibbons, Phys. Rev. **159**, 1007 (1967).

[41] U. Abbondanno *et al.*, Nucl. Instrum. Meth. A **521**, 454 (2004).

[42] J. Lerendegui-Marco *et al.*, A GEANT4 application for planning and analysis of C_6D_6 capture measurements at n_TOF, n_TOF Public Note, May 2015.

[43] J. L. Taín and D. Cano-Ott, Nucl. Instrum. Meth. A **571**, 719 (2007).

[44] *Evaluated Nuclear Structure Data File*, National Nuclear Data Center, Brookhaven National Laboratory.

[45] J. Kopecky and M. Uhl, Phys. Rev. C **41**, 1941 (1990).

[46] T. A. Laplace, F. Zeiser, M. Guttormsen, A. C. Larsen, D. L. Bleuel, L. A. Bernstein, B. L. Goldblum, S. Siem, F. L. Garotte, J. A. Brown, L. C. Campo, T. K. Eriksen, F. Giacoppo, A. Gorgen, K. Hadynska-Klek, R. A. Henderson, M. Klintefjord, M. Lebois, T. Renstrom, S. J. Rose, E. Sahin, T. G. Tornyi, G. M. Tveten, A. Voinov, M. Wiedeking, J. N. Wilson, and W. Younes, Phys. Rev. C **93**, 014323 (2016).

[47] M. Barbagallo *et al.* (The n_TOF Collaboration), Eur. Phys. J. A **49**, 156 (2013).

[48] N. M. Larson, ORNL/TM-9179/R8, ORNL, Oak Ridge, Tennessee, USA (2008).

[49] G. F. Auchampaugh *et al.*, Phys. Rev. C **7**, 2085 (1973).

[50] H. Weigmann *et al.*, Nucl. Phys. A **438**, 333 (1985).

[51] J. L. Ullmann, T. Kawano, B. Baramsai, T. A. Bredeweg, A. Couture, R. C. Haight, M. Jandel, J. M. O'Donnell, R. S. Rundberg, D. J. Vieira, J. B. Wilhelmy, M. Krticka, J. A. Becker, A. Chyzh, C. Y. Wu, and G. E. Mitchell, Phys. Rev. C **96**, 024627 (2017).

[52] C. E. Porter and R. G. Thomas, Phys. Rev. **104**, 483 (1956).

[53] E. P. Wigner, Conference on Neutron Physics by Time-of-Flight, Gatlinburg, Tennessee, 1956, Oak Ridge National Laboratory Report No. ORNL-2309, 59 (1957).